MODELLING YOUNG STAR CLUSTERS WITH AMUSE

MODELLING YOUNG STAR CLUSTERS WITH AMUSE

By

JESSICA MCCLOSKEY, B.SC. SPEC. HON., UNIVERSITY OF OTTAWA, 2013

A Thesis

Submitted to the School of Graduate Studies

in Partial Fulfillment of the Requirements

for the Degree

Masters of Science

McMaster University

MASTERS OF SCIENCE (2015)   McMaster University

(Physics and Astronomy)   Hamilton, Ontario

TITLE: Modelling Young Star Clusters with AMUSE

AUTHOR: Jessica McCloskey, B.Sc. Spec. Hon., University of Ottawa, 2013

SUPERVISOR: Alison Sills

NUMBER OF PAGES: ix, 87

Abstract

An important research area in modern astrophysics is understanding how molecular clouds form stars and star clusters. These rich clusters within molecular clouds are the dominant mode of star formation in our galaxy, but we know very little about these areas of space due to incomplete observational data. The MYStIX (Massive Young Star-Forming Complex Study in Infrared and X-Ray) project was started to create a detailed catalogue of these regions and the rich star clusters embedded within them. Once the observational data was available, the evolution of these clusters could be investigated in more detail. Current cluster simulations investigate the stars in detail but usually ignore the gas entirely which can be inaccurate, especially in gas mass dominated clusters. We use AMUSE (Astrophysical Multi-purpose Software Environment) to model embedded young clusters with stars and gas, similar to those found by the MYStIX project, and track their evolution over the first few million years of their lifespan while allowing the stars and gas to interact. We are particularly interested in non-spheroidal subclusters and how they can evolve into the spherical structures that we see today.

Acknowledgements

I'd first like to thank my supervisor, Alison Sills, for being extraordinarily patient with me as I dove into real astronomy for the first time. Thank you for both your guidance and your support, these last two years have been a wonderful experience.

Thanks to my officemates for making me laugh even when I had a draft due the next morning and I hadn't slept in two days.

And to my family, and especially my parents, thank you for the unwavering support and love you've given me all my life, I never could have done this without you.

Contents

3 Method and Results   57

4 Discussion & Conclusion   75

List of Figures

List of Tables

Chapter 1

Introduction

For my part I know nothing with any certainty

but the sight of the stars makes me dream.
— Vincent van Gogh

In this thesis, we are studying the evolution of very young, dense star clusters during their early stages when they are still embedded in their natal gas. In particular, we are looking at how the shape of these clusters can change quickly over time at this stage.

In this chapter, we will describe the observations that influenced and motivated the creation of this project as well as what questions arose from this data.

1.1 Observations of Young Star Clusters

1.1.1 Studies of Young Stellar Clusters

In recent years, the study of star formation has been advanced in molecular clouds (regions of molecular gas and dust with masses ranging from 10^3 to 10^7 solar masses, often with substructure of voids, filaments and clumps), with millimeter and infrared studies of nearby clouds to accurately view the stages of star formation from gravitational collapse to protostars (Burkert, 2002; Fukui, 2002). These nearby clouds mainly form stars of intermediate mass (between 0.8 and 10 solar masses) to cool brown dwarfs (between 13 and 80 Jupiter masses).

While this field has progressed, the understanding of star formation within massive star forming regions (MSFRs) has remained relatively rudimentary. This is especially important with regards to rich star clusters, as they are thought to be a main, possibly dominant, mode of star formation within our galaxy (Allen et al., 2007).

Some of the outstanding questions include:

- What are the essential conditions for rich cluster formation and how do those conditions can arise?

- Do all stars within a cluster form at the same time or is star formation active for a more prolonged period (multiple Myrs)? How would this affect the gas within the young cluster?

- What are possible causes of mass segregation? Mass segregation is a process

by which the higher mass stars of a cluster lose velocity and move toward the centre of the cluster, which will be discussed in more detail in Section 2.2;

- Are larger rich clusters formed from the mergers of smaller clusters? This is supported by a more advanced stage of mass segregation observed in a cluster than is expected from its age and relaxation time (Fujii et al., 2012), but this apparent inconsistency could also be caused by an initial mass segregation in the system (McMillan et al., 2007);

- What does the detailed structure of rich clusters look like? Are they the smoothed distributions most commonly used to model them, or is there a complex substructure underneath?

These issues, among others, could be better resolved if there existed a more complete and detailed data set on these MSFRs and rich clusters. Even though their existence has been known for many years, only the closest of the rich clusters (Orion Nebula Cluster) even has a full Initial Mass Function (a function that describes the initial distribution of masses in a population of stars, see Section 2.6 for further details) determined (Pflamm-Altenburg and Kroupa, 2006), with many clusters having only incomplete censuses.

There are technical reasons behind this lack of data, it was not a lack of motivation. Emission from heated dust and gas, overcrowding from the field stars (there can exist a hundred times more field stars in the area of interest than cluster members), and spatial obscuration from the molecular cloud itself were all difficulties encountered when trying to study rich clusters. This resulted in a restricted sample of mostly

partially obscured OB stars (hot, massive stars that emit mainly in the ultraviolet range, burning bright and quickly and so easily to see than smaller, dimmer stars), or young stars with protoplanetary disks that would give off excess infrared radiation. Surveys would completely miss young, disk-free, low-mass to intermediate-mass stars that usually dominate the populations of young clusters (Feigelson et al., 2013).

The Spitzer Young Cluster survey used the mid-infrared range to identify 2548 young stellar objects in 36 nearby star-forming clusters and groups, including embedded clusters, but was unable to characterize (identify or include in spatial distribution and surface density analysis) any diskless stars or stars without an excess of infrared (Gutermuth et al., 2009).

Since these problems mainly plagued optical and infrared studies, the use of X-Ray telescopes (such as the Chandra X-Ray Observatory) can be used to differentiate young stars within a cluster at distances up to 4 kpc (Feigelson, 2010). This can be supplemented by optical and infrared observations to ensure that all sources remain Galactic and there is no contamination by extra galactic sources.

1.1.2   MYStIX

The Massive Young Star-Forming Complex Study in Infrared and X-ray (MYStIX) (Feigelson et al., 2013) is a study, based at Pennsylvania State University, that combines a variety of surveys into a more complete census. The wavelengths used include the optical band for OB stars, infrared bands for young stars with protoplanetary disks and X-ray bands for both OB stars and young, disk-free, low-mass

and intermediate-mass stars. Beyond just the stars, once the data was cleaned of contamination from non-cluster sources, the diffuse plasma from OB stars and the remnants of supernovae were also visible in the X-ray bands.

The data used by MYStIX include:

- archival X-ray data from NASA's Chandra X-ray Observatory;

- near-infrared data from the United Kingdom InfraRed Telescope (UKIRT);

- near-infrared data from the Two Micron All Sky Survey (2MASS);

- and mid-infrared data from NASA's Spitzer Space Telescope.

The purpose of MYStIX was to create a census of cluster members, with as uniform an analysis procedure as possible, reducing incompleteness and selection biases, and using more than one classification method to ensure objective selection of sources. Although there exist past studies on most of the individual local MSFR's, it is difficult to compare these findings, as they all used different methodologies and datasets that could sometimes contradict and disallow valid comparisons. While MYStIX's collection of clusters is diverse and without a well-defined characteristic to refine the sample, its consistent methodologies and compatible datasets allow for collection-wide investigation of their properties.

The study produced a census with 31,784 identified MYStIX Probable Complex Members (MPCMs, stellar members of the MSFRs) within the 20 MSFRs targeted by the surveys (Broos et al., 2013). This makes MYStIX the largest survey of rich star forming regions to date.

The project aimed to investigate:

- single-wavelength analysis of X-ray, near-infrared and mid-infrared data;

- matching X-ray and infrared sources;

- classification of X-ray sources;

- a new stellar age estimator and star formation histories of MSFRs;

- new OB stars;

- and spatial clustering of MPCM stars.

It is this last item which forms the basis for this thesis.

1.1.3   Spatial Clustering

Both the star formation process and dynamical evolution of a cluster can have an effect on the spatial distribution of its stars. If, as suggested by Elmegreen (2000), star formation happens within a crossing time (the time required for a star in a cluster travelling at the average velocity, to cross the cluster), then the distribution of the stars would be similar to the structure of the initial cloud. If conversely, as suggested by Tan et al. (2006) and Howard et al. (2014), there is gradual star formation throughout a cluster's lifetime, then a smoother stellar density map will emerge. So, investigating the structure of rich star clusters is important to understanding their creation and evolution.

There are multiple difficulties associated with determining and comparing the structure of clusters. Different clusters that have undergone different processes can produce similar properties (the merging of two subclusters can appear as a young single cluster due to their different relaxation mechanisms (Allison et al., 2009); various methods of gas removal may produce similar results (Moeckel and Bate, 2010)), so more than one evolutionary path must always be considered. There are difficulties in determining exactly which stars are cluster members and which are merely surrounding field stars (Pfalzner et al., 2012), so densities beyond just the stellar distribution (such as the molecular clouds) must be investigated and reasonable boundaries must be determined. The sheer number of morphologies and properties that are all plausible for star clusters can make it difficult to reasonably compare a random sample such as the MYStIX sample, so a large amount of information must be available to compare different regions quantitatively.

Another area of discussion is how to properly characterize the stellar densities of these clusters. While the Plummer sphere (a density law describing observations of globular clusters, with a near-constant-density core, for more information see Section 2.6) is widely used as a model for the distribution of stars, some have noted that for clusters like Orion Nebula Cluster, NGC 6611, W 40, and Tr 15, a King profile (another density law to describe clusters, but with a parameter that changes the form of the profile allowing for extended envelopes if desired) might suit them better, with their higher ratios of half-mass radius to core radius (Pfalzner et al., 2012).

However, no matter what smooth distribution would be most ideal, it remains that young clusters may not have had enough time to fully dynamically relax into

one of these profiles though two-body interactions and that the presence of molecular gas could change the gravitational potential enough to affect the stellar distribution. It can also be seen that for many of the cluster regions, there are smaller groups of stars either surrounding the main cluster or as subclusters within the main cluster.

When looked at uniformly, the MYStIX sample displayed a variety of types of substructure: sometimes dominated by a single monolithic cluster, sometimes a dominant cluster with substructure, sometimes several clusters, and sometimes a dominant cluster with secondary subclusters (Kuhn et al., 2014). To identify the subclusters in the raw data, a method of cluster analysis had to be chosen. Kuhn et al. (2014) decided upon a parametric method that involved assuming that the populations were made up of subclusters with elliptical surface-density distributions, and that the mixture model is the sum of these densities. The properties of these subclusters were determined by maximum-likelihood estimation.

In this parametric method, the models of the young clusters were based on equilibrium configurations of self-gravitating stars in the form of isothermal ellipsoids (Chandrasekhar, 1942). The density profile of an isothermal sphere can be approximated by using the Hubble model:

$$\Sigma(r) = \frac{\Sigma_0}{1 + (r/r_c)^2} \tag{1.1}$$

where $\Sigma(r)$ is the surface density at a distance r from the cluster centre, Σ_0 is the central surface density, and r_c is the core radius. We can also find the central volume

density using the central surface density:

$$\rho_0 = \frac{\Sigma_0}{2r_c} \tag{1.2}$$

and the number of stars N projected within r can be expressed as:

$$N(<r) = \pi r_c^2 \Sigma_0 \ln(1 + r^2/r_c^2) \tag{1.3}$$

In order to use this to model an ellipical shape, as very few clusters are perfectly spherical (indeed, the Orion Nebula cluster has an ellipticity of $\epsilon \simeq 0.3$), the Hubble density profile must be 'stretched' to include two new parameters: the ellipticity $\epsilon = (a - b)/a$ (where a and b are the semi-major and semi-minor axes respectively) and the ellipse orientation ϕ.

$$\Sigma_{ell}(\mathbf{r}; \Sigma_0, r_0, r_c, \phi, \epsilon) = \Sigma_0 \left[1 + \left| \begin{pmatrix} (1-\epsilon)^{-1/2} & 0 \\ 0 & (1-\epsilon)^{1/2} \end{pmatrix} \hat{R}(\phi)(\mathbf{r} - \mathbf{r}_0) \right|^2 \Big/ r_c^2 \right]^{-1} \tag{1.4}$$

where $\hat{R}(\phi)$ rotates the vector $\mathbf{r} - \mathbf{r}_0 \equiv (x - x_0, y - y_0)$ by angle ϕ.

The study identified 142 subclusters within 17 of the MYStIX MSFRs, and Kuhn et al. (2014) gives the celestial coordinates for the cluster centre, semi major and semi minor axes of the core ellipse, ellipticity, orientation, and the total number of stars in the ellipse four times the size of the core.

Figure 1.1 shows the distribution of cluster core radii. This is fit by a lognormal

distribution with a mean of 0.17 pc, with 68% of the core radii between 0.06 and 0.45 pc. The edges of this distribution are not well constrained, as the smallest values are for very sparse clusters without a proper core, and the largest values are for broad stellar overdensities that do not form distinct subclusters. So, a bias may be present in the data, as the clusters with the largest MYStIX distance have larger radii, as in the overdensities of these regions, distinct subclusters might appear to have merged to create larger artificial subclusters. However, even with those tails discarded, the most common size of cluster is consistent for all MYStIX distances.

Figure 1.2 is a plot of the cluster core radii against the absorption along line of sight, for X-ray energy median energy (ME) (right) and J - H (left). The X-ray energy ME can be used as a measure of absorption, as it corresponds reliably with the log of the line-of-sight column density (Getman et al., 2010). A negative correlation can be seen in both these plots, emphasizing that the more embedded clusters are smaller, with subclusters with a median ME > 2.5 keV rarely having a core radius above 0.2 pc. Previous studies have shown that embedded clusters lose their gas as they age (Lada and Lada, 2003; Leisawitz et al., 1989), so this negative relation can also be used to show a positive size-age relation, indicating that clusters, or at least their cores, expand as they age.

Figure 1.3 (left) shows a histogram of the ellipticities of the MYStIX clusters, indicating a range in ellipticities from 0 to ~ 0.8, with a preference toward lower ellipticities. It can also be seen in the right side of the figure that a cluster's ellipticity does not depend on its core radius. Previous studies have shown that a molecular cloud with a high ellipticity is highly susceptible to instability due to gravitational
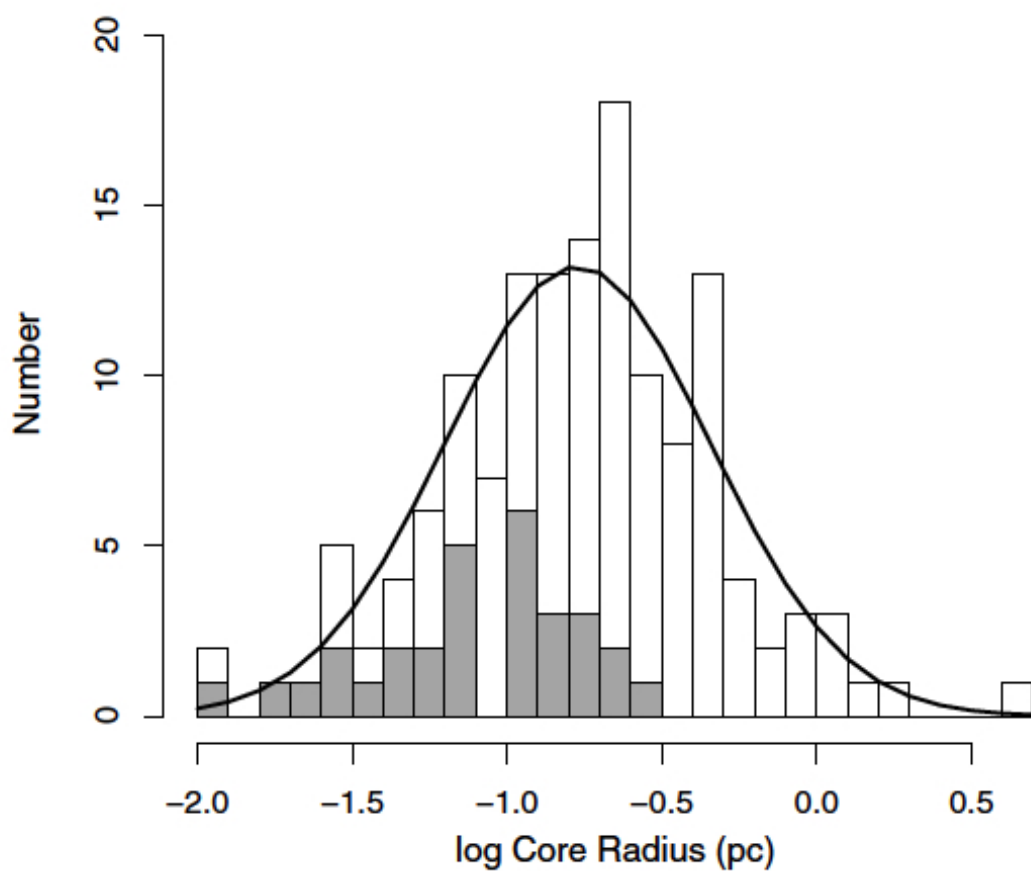
Figure 1.1: Histogram of cluster core radii for all subclusters (white) and embedded clusters (grey). (Kuhn et al. (2014) ©AAS. Reproduced with permission)

fragmentation (Burkert and Hartmann, 2004). This is not contradicted in this study, as MYStIX clusters with the highest ellipticities may not be for distinct subclusters, but be part of a larger complex that include unclustered stars, falsely inflating their ellipticity values.

While there is a large variety in the subcluster structure amongst the sample, it is possible to divide them into four general classes.

Simple Isolated Cluster Structure. As its name suggests, this is the simplest of the classes, with the cluster dominated by a single ellipsoid model. Perhaps because of this simplicity, these clusters are also generally the most dynamically relaxed clusters. And although this more advanced relaxation might suggest older clusters, it was found that the regions of this class were not always the oldest, some still experiencing star formation. In Figure 1.4 we can see examples of this class that include the Flame Nebula (slightly elongated in the direction of the filamentary cloud), W 40 (round), and the principal clusters in the Trifid Nebula.

Core-Halo Structure. This class consists of clusters that seem unimodal, but do not fit the single ellipsoid model due to an excess of stars at the centre (or lack of stars near the edges). A better fit for these clusters is to use two ellipsoids, one at the centre of the cluster to model the core and one surrounding it to model the halo. In Figure 1.5, we can see examples of this class that include the Orion Nebula Cluster, RCW 36, and RCW 38 (which looks different than the others due to its core being off-centre from its halo).

Clumpy Structure. Not all the MYStIX regions were easily fit by discrete ellipsoids
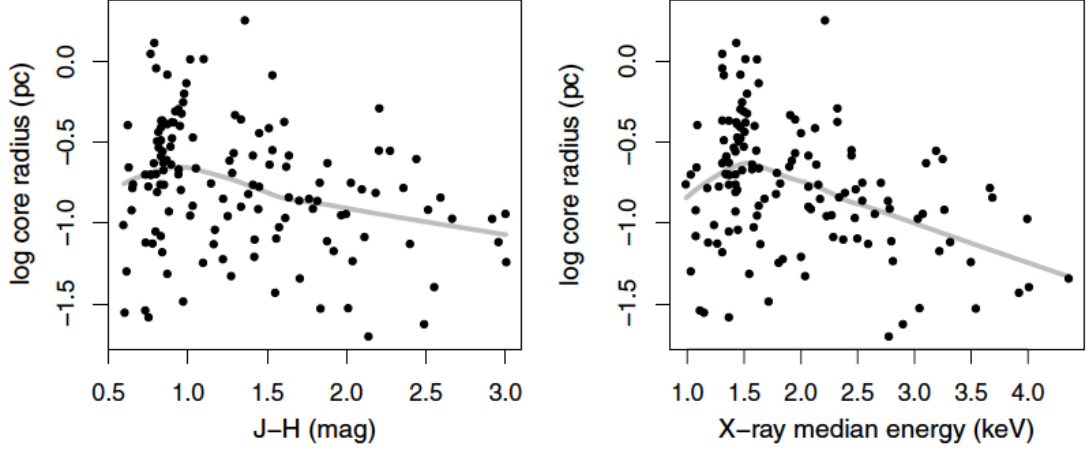
Figure 1.2: Relation of cluster core radii to absorption along line of sight for median J - H mag (left) and median X-ray median energy in the 0.5-0.8 keV band (right) (Kuhn et al. (2014) ©AAS. Reproduced with permission)
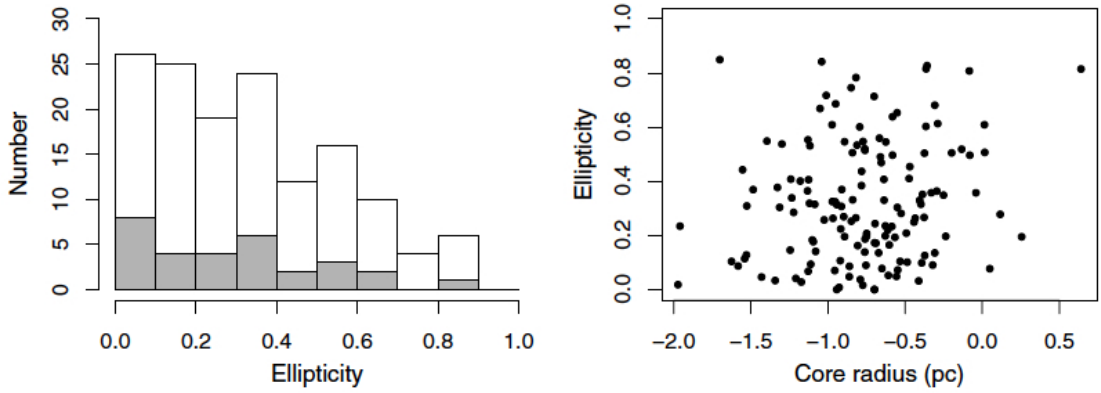
Figure 1.3: *Left:* Histogram of cluster ellipticities for all subclusters (white) and embedded clusters (grey). *Right:* Scatter plot of subcluster core radii vs. ellipticity. (Kuhn et al. (2014) ©AAS. Reproduced with permission)

Figure 1.4: Smoothed projected stellar density maps with colour bar in units of observed stars pc^{-2} for Simple Isolated Cluster Structure. *Upper left:* Trifid, *upper right:* Flame Nebula, *lower left:* W 40 (Kuhn et al. (2014) ©AAS. Reproduced with permission)

Figure 1.5: Smoothed projected stellar density maps with colour bar in units of observed stars pc^{-2} for Core-Halo Structure. *Upper left:* Orion Nebula, *upper right:* RCW 36, *lower left:* RCW 38 (Kuhn et al. (2014) ©AAS. Reproduced with permission)

because of the clumpy nature of their structure. They might have a dominant central subcluster, but a significant portion of the stars lie outside these bounds in secondary subclusters. In Figure 1.6, we can see examples in M 17, the Lagoon Nebula and the Eagle Nebula.

Linear chains of clusters. This class consists of regions where subclusters are arranged generally along a line. The stars are separated along this line, broken up into subclusters as opposed to being in a continuous distribution. Although it would seem obvious that the subclusters would be oriented so that they would be elongated along the long axis of the filament, this is not always the case though it is more common than the alternative. Of note is the fact that the young stars in the region are very evenly distributed amongst the subclusters, with no subcluster containing more than 20% of the MPCMs within 5 core radii. In Figure 1.7, we can see examples of this class in NGC 2264, NGC 1892, NGC 6334, and DR 21, which are all embedded within molecular clumps.
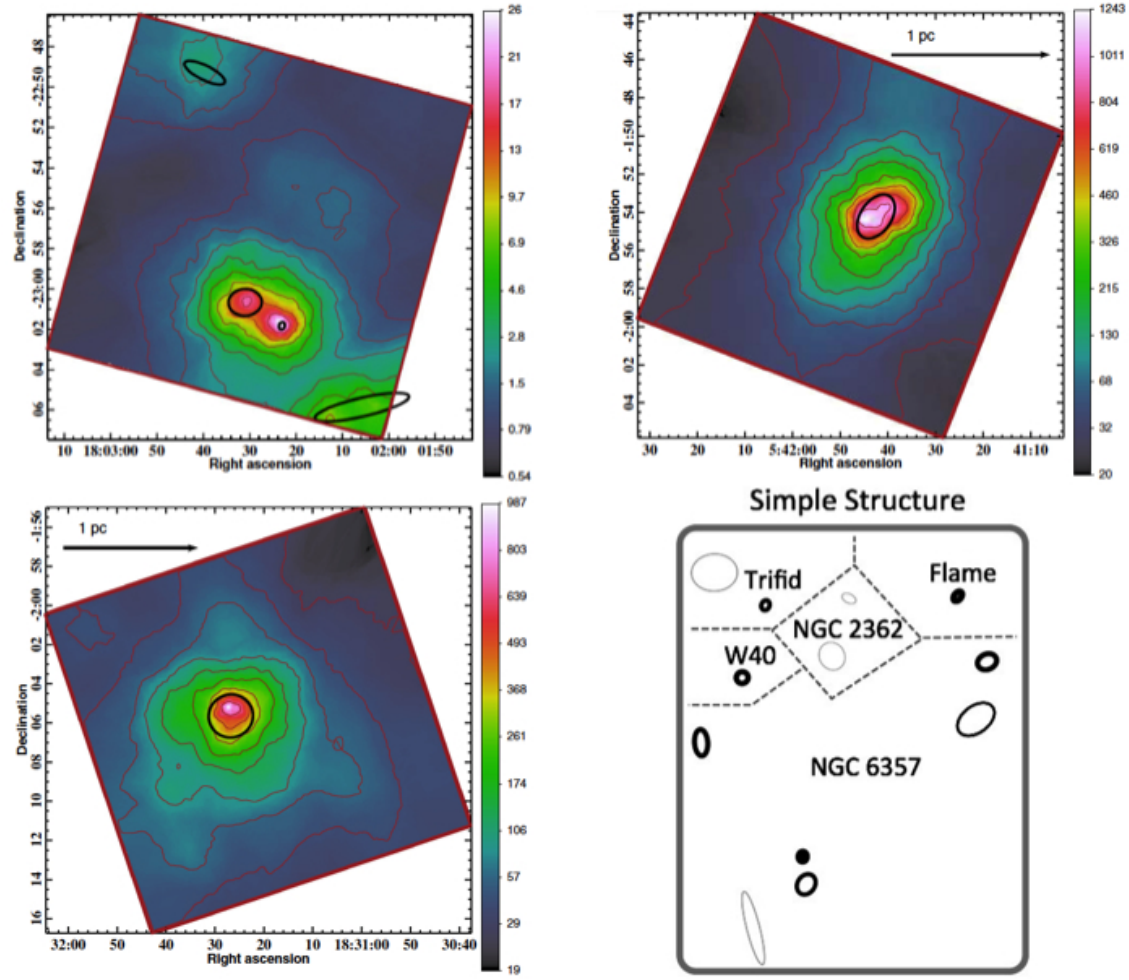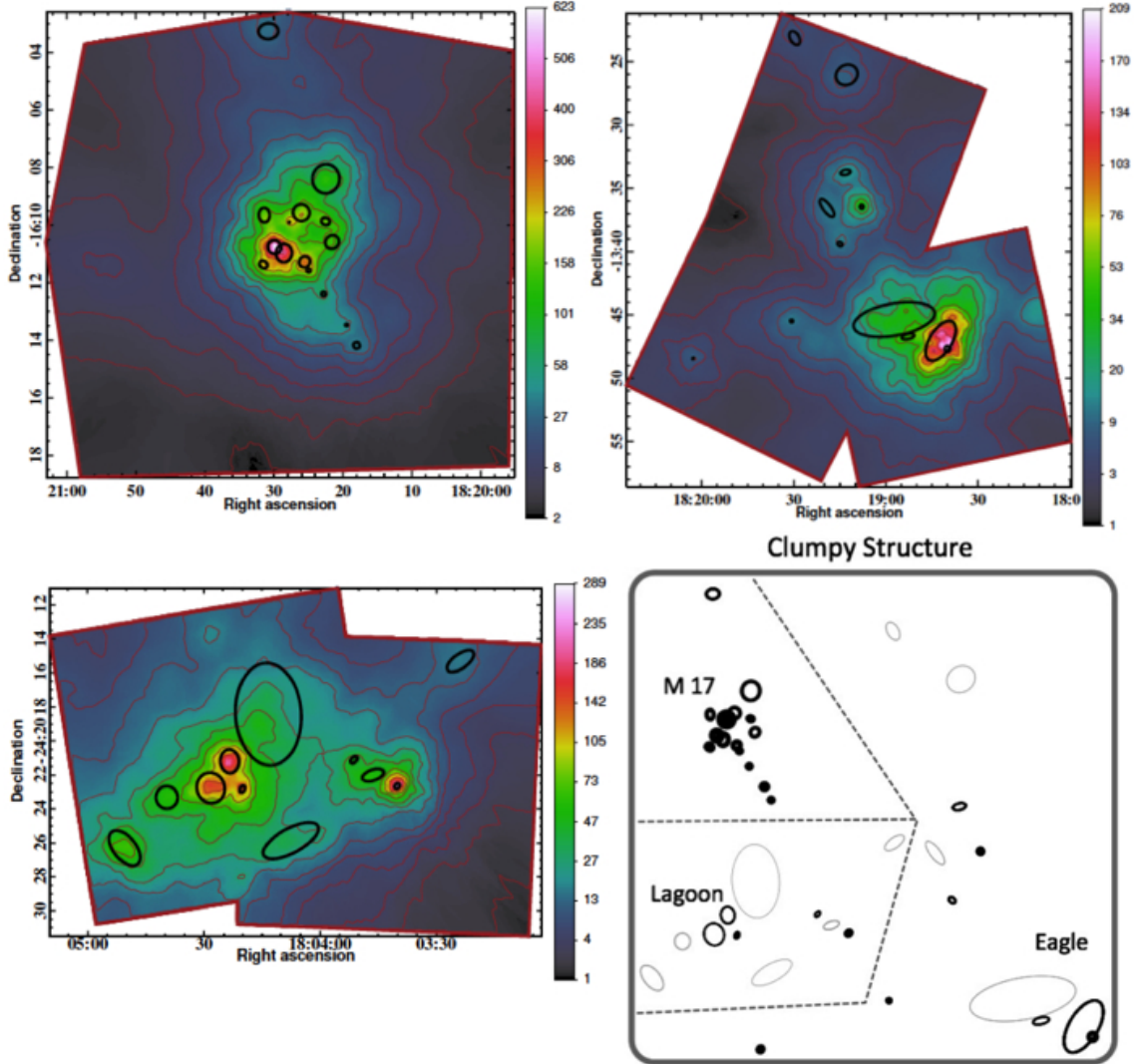
Figure 1.6: Smoothed projected stellar density maps with colour bar in units of observed stars pc^{-2} for Clumpy Structure. *Upper left:* M 17, *upper right:* Eagle Nebula, *lower left:* Lagoon Nebula. (Kuhn et al. (2014) ©AAS. Reproduced with permission)
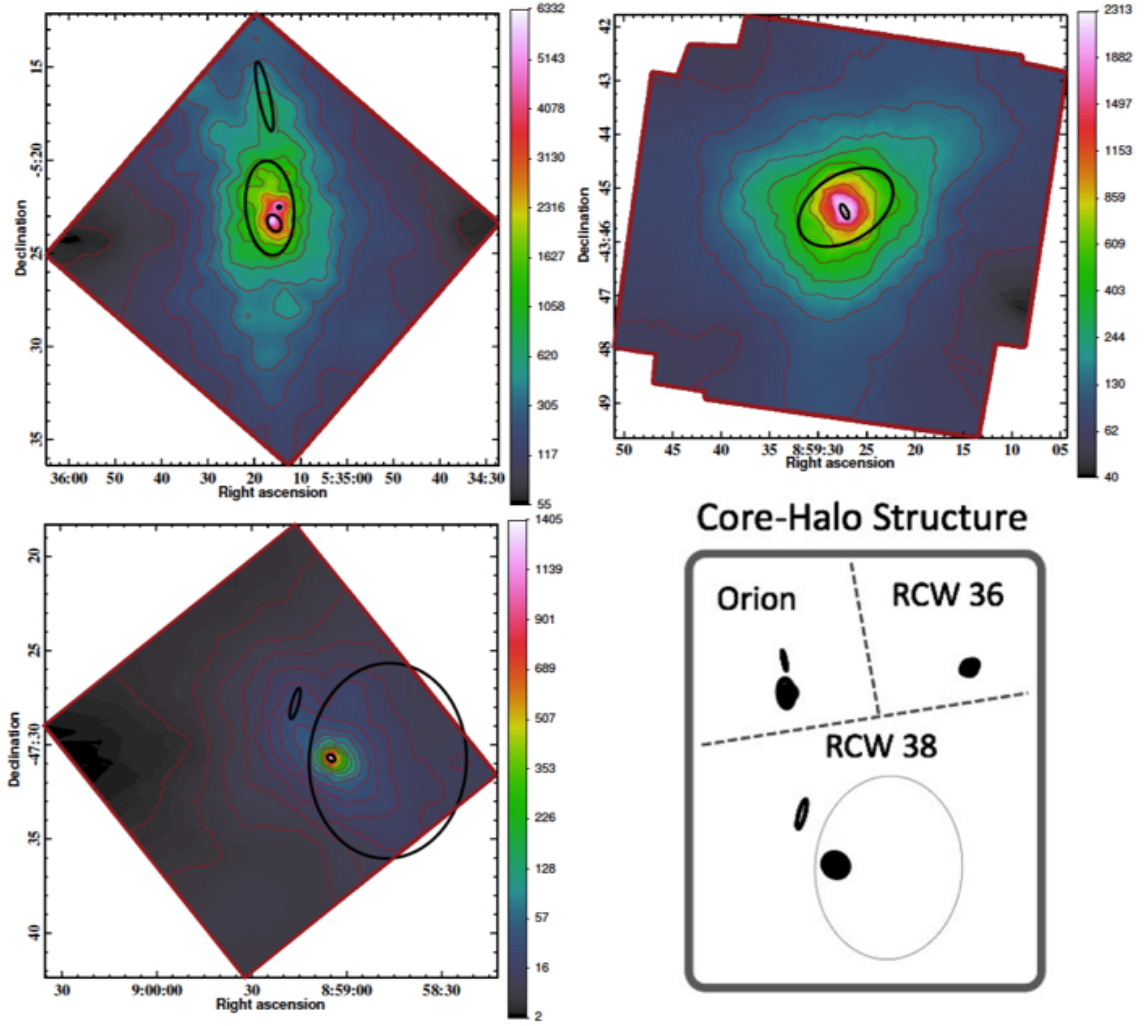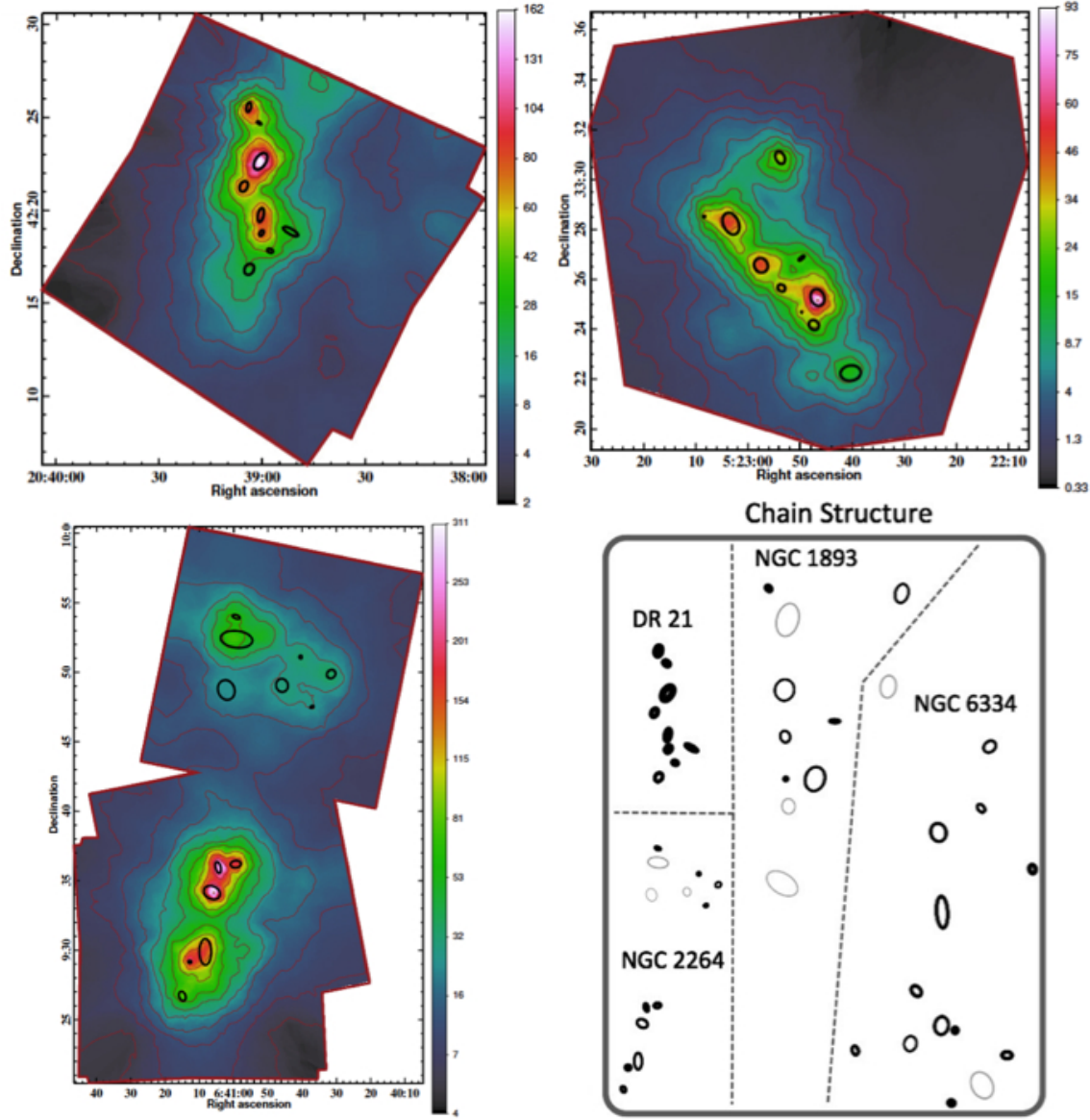
Figure 1.7: Smoothed projected stellar density maps with colour bar in units of observed stars pc^{-2} for Linear chains of clusters. *Upper left:* DR 21, *upper right:* NGC 1893, *lower left:* NGC 2264. (Kuhn et al. (2014) ©AAS. Reproduced with permission)

1.2 Motivation

Now that we have these observations, we can ask some interesting questions about the early evolution of star clusters.

- How do these young embedded clusters evolve, with their high ellipticity and large fraction of gas mass?

- Is the lack of older elliptical clusters due to evolution or dissipation of the young clusters?

- How does the presence of this gas affect the clusters, and how might this affect how we look at gas expulsion?

In this thesis, we will be primarily be focussing on the ellipticities of the MYStIX clusters, investigating through computer simulations if these highly elliptical clusters can evolve into the spherical older clusters we normally see.

We will also be working with embedded clusters, keeping the gas in the simulation for the full duration, not immediately expelling it through a large injection of energy (as seen in Bastian and Goodwin (2006)) or initializing our simulation without gas entirely (as seen in Pfalzner et al. (2012)).

Chapter 2

Computational Methods

2.1 Introduction

In this section, we describe the computational methods used within this thesis as well as some of the physics behind the interactions of both stars and gas.

We outline the basics of stellar dynamics, tree codes, and SPH codes as well as the specific codes used in this research - hermite0, BH Tree and GADGET-2. We also present a description of the Bridge and AMUSE codes and frameworks. Section 2.1 is largely a summary of the stellar dynamics introduction from Binney and Tremaine (2008), and Section 2.2 draws heavily from Pfalzner and Gibbon (1996).

2.2   Stellar Dynamics

Stellar dynamics describes the gravitational interactions of point mass particles in a system. These N-body systems can be on the scale of open clusters ($10^2 - 10^3$ stars) to globular clusters ($10^4 - 10^5$ stars) to galaxies (10^{12} stars). On an even larger scale, instead of representing stars, the discrete particles can represent galaxies to describe the interactions of galaxies within a cluster.

Within a N-body system, gravity is the only truly important force, and in most cases, Newton's approximations are valid (except for in situations like near the event horizon of a black hole, where general relativity is required). This means that the general equations of motions are as follows,

$$\dot{\mathbf{r}}_i = \mathbf{v}_i \tag{2.1a}$$

$$\dot{\mathbf{v}}_i = -G \sum_{j=1,\neq i}^{N} m_j \frac{\mathbf{r}_i - \mathbf{r}_j}{|\mathbf{r}_i - \mathbf{r}_j|^3} \tag{2.1b}$$

An isolated system (i.e. without outside forces or interaction) must conserve energy and have a balance of kinetic and potential energy. If a system had no kinetic energy (i.e. no independent movement of particles), then it would collapse in on itself, so for a system to remain in equilibrium, it must have both potential and kinetic energy. There are two main ways the kinetic energy is stored: 1) ordered, i.e. rotation of a disk in a spiral galaxy and 2) random, pressure supported, i.e. elliptical galaxy or star cluster. As we are looking at stellar clusters, pressure-supported systems are of far more interest.

In an N-body system, the most basic process in the system is the acceleration of each star as a result of its gravitational interaction with every other star in the system.

If we follow a subject star on its orbit around a cluster and it passes another star along its trajectory at a distance b (also termed the distance of closest approach) and we compare the subject star's initial trajectory to its new trajectory after being exposed to the field star, we will find a difference in its velocity $\delta \mathbf{v}$, where we assume that $|\delta \mathbf{v}|/v \ll 1$ and that the field star is stationary. To determine $\delta \mathbf{v}$ we must first look at the force caused by gravity that is perpendicular to the motion of the star, taking t=0 as the instant the stars are b distance apart as in Figure 2.1.

$$F_\perp = \frac{Gm^2}{b^2 + x^2} \cos \theta = \frac{Gm^2 b}{(b^2 + x^2)^{3/2}}$$

$$= \frac{Gm^2}{b^2} \left[1 + \left(\frac{vt}{b} \right)^2 \right]^{-3/2} \tag{2.2}$$

And since we know from Newton's Laws that $m\dot{\mathbf{v}} = \mathbf{F}$, then we can also say that

$$\delta v = \frac{1}{m} \int_{-\inf}^{\inf} dt F_\perp = \frac{Gm^2}{b^2} \int_{-\inf}^{\inf} \frac{dt}{[1 + (vt/b)^2]^{-3/2}}$$

$$= \frac{2Gm}{bv} \tag{2.3}$$

This perturbation is not a significant one on its own, and though the subject star is travelling through a large number of field stars and thus experiences a large number of interactions, since the stars are randomly situated, the average $\delta \mathbf{v}$ will still be close

to zero. However, the *mean-square change* does not go to zero and after one crossing of the system, where δn is the number of encounters the subject star undergoes from b to $b + \mathrm{d}b$,

$$\sum \delta v^2 \simeq \delta v^2 \delta n = \left(\frac{2Gm}{bv}\right)^2 \frac{2N}{R^2} b\, \mathrm{d}b \tag{2.4a}$$

$$\Delta v^2 = \int_{b_{min}}^{b_{max}} \sum \delta v^2 \simeq 8N \left(\frac{Gm}{Rv}\right)^2 \ln \frac{b_{max}}{b_{min}} \tag{2.4b}$$

This means that the mean-square velocity will increase from its original value as a function of the number of encounters it undergoes, which can also be related to the time. The typical speed of a star at the edge of the system can be defined as

$$v^2 \approx \frac{GNm}{R} \tag{2.5}$$

And if we use this equation to replace R in equation (2.4b),

$$\frac{\Delta v^2}{v^2} \approx \frac{8 \ln \frac{b_{max}}{b_{min}}}{N} \tag{2.6}$$

For every crossing of the cluster, the star's velocity v will change by Δv^2, so we can find the number of crossings necessary to produce $(\Delta v^2) = v^2$ using

$$n_{relax} \simeq \frac{N}{8 \ln \frac{b_{max}}{b_{min}}} \tag{2.7}$$

From these equations, we can get the stellar dynamical *relaxation time*, which

is the time required for the cumulative encounters to modify the velocity of the subject star by approximately its initial value. It can be defined as $t_{relax} = n_{relax} t_{cross}$ where $t_{cross} = R/v$ is the crossing time, or the time needed for a single star to cross the entire system. If we assume that the system is near equilibrium, then taking $\frac{b_{max}}{b_{min}} \approx Rv^2/Gm$, due to our assumption of straight-line trajectories and also the homogeneous distribution of field stars,

$$t_{relax} = \frac{0.1N}{\ln N}\frac{R}{v} = \frac{0.1N}{\ln N}t_{cross} \tag{2.8}$$

These interactions between subject and field stars cause a diffusion of velocity separate from the average acceleration from the mass distribution of the system. This is called *two-body relaxation*, since it is based on the cumulative two-body interactions the subject star experiences.

There are two main types of dynamical systems in an astrophysical context: *collisional* and *collisionless*. Systems where $t_{relax} \gg t_{cross}$ are called collisionless, because the essentially smooth gravitational potential dominates the orbits of the particles in the system. Other systems where local perturbations in the gravitational forces dominate the orbits are called collisional, due to the large angle scattering these perturbations can cause. Generally, collisional systems are smaller and denser, than collisionless systems. It is possible for the stars to physically collide, but this happens rarely and only in the most dense stellar system. In this thesis, our star clusters were collisional, as the relaxation time was not orders of magnitude larger than the crossing time (indeed, the code we use, *hermite0* discussed in section 2.2.1 is suited

best to collisional systems (Pelupessy et al., 2013)).

We can also define the evaporation time, t_{evap}, or the time required for a significant number of stars to leave the system. Generally, $t_{evap} \approx 100 \, t_{relax}$ for isolated systems. For systems like globular clusters, this timescale is on the order of 200 billion years if the cluster is in isolation, and can be significantly shorter if the cluster is in the tidal field of a galaxy.

Another important factor to consider in stellar dynamics is *equipartition*, where in an encounter, an object with higher kinetic energy will lose energy to an object with lower kinetic energy, leaving them with equal energy. And since kinetic energy is proportional to the square of the speed multiplied by the mass, a small object must have a higher velocity than a large object to have the same kinetic energy. In a typical stellar cluster, there will be stars of varying masses; so if a larger and a smaller star have an encounter, the larger star will end up with a lower velocity than the smaller star. This leads to the smaller stars in a cluster moving to higher orbits and drifting to the edges of the cluster, while the larger mass stars move to lower orbits and stay closer to the centre. This separation of different masses of stars is known as *mass segregation*.

In the core of a cluster, the stars will have higher velocities and as these stars undergo equipartition, this loss of kinetic energy will cause them and other heavy stars to sink further toward the centre of the cluster. The limit of this process is called *core collapse*, though it is often halted or even reversed by the injection of energy that comes from interactions with binary stars. If there are three stars in a

system, labeled $i = 1, 2, 3$, and the first two stars create a binary, then that binary's kinetic energy can be labeled K_b and its internal energy $E_b < 0$ and the third star's kinetic energy is K_3'. Since energy must be conserved,

$$K_b + E_b + K_3' = K_1 + K_2 + K_3 \tag{2.9a}$$

$$K_b + K_3' > K_1 + K_2 + K_3 \tag{2.9b}$$

The kinetic energy stored in the centre of mass of the binary and the third star is larger than the kinetic energy of the initial system. This means that the formation of binary stars is actually a heat source for the cluster. This addition of energy is enough to halt the process of core collapse, as all clusters possess binaries, and even if these binaries are not primordial, the core collapse process creates them.
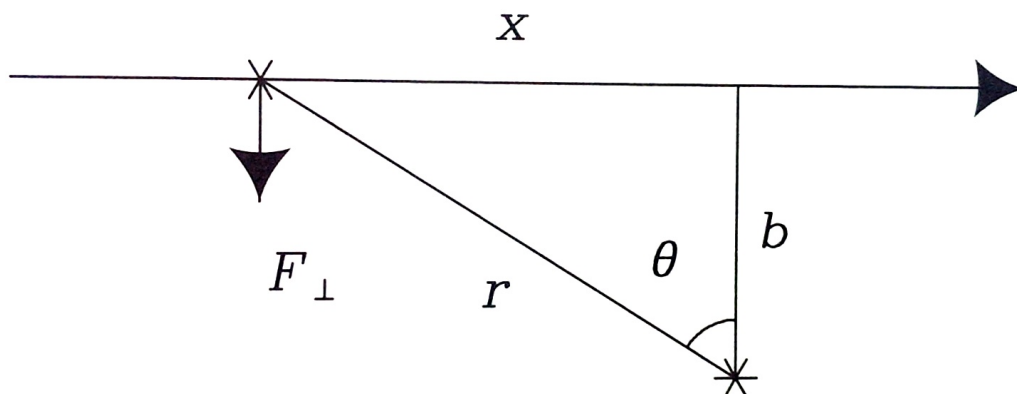
Figure 2.1: The subject star approaching a field star. The trajectory is approximated using a straight line, with the distance of closest approach b, the distance r, and the perpendicular force $F_\perp$. (Binney and Tremaine (2008) Reprinted with the permission of Princeton University Press.)

2.2.1   Hermite0

An N-body code must contain at least three separate parts: initial conditions, integrator, and data analysis. In this section we will be discussing one particular integrator, the Hermite scheme. Since direct summation of the acceleration of particles in a system ends up taking $O(N^2)$ time, where N is the number of particles, and this ends up being very costly if performed at every integration step, there needed to be a faster way to calculate these values.

The code *hermite0* is based on a modification of the leapfrog method (Hockney and Eastwood, 1988), where the positions and velocities are calculated on alternating half-timesteps.

$$r_1 = r_0 + v_{1/2}\Delta t \tag{2.10a}$$

$$v_{3/2} = v_{1/2} + a_1\Delta t \tag{2.10b}$$

While this scheme is simple and easy to code, it is not always accurate enough and the constant timesteps were impractical considering the time length some applications needed. Additionally, since many applications involve situations where only a few particles are being influenced by nearby particles, so their timesteps need to be short, but at the same time, the vast majority of the particles are not moving or interacting. So with a constant timestep, the whole system needs to be evaluated all the time, which is inefficient considering that much of the system remains the same between timesteps. These repeated unnecessary calculations also lead to a possible build up of numerical errors.

For convenience, a 'flattened' version of the above equations can be used, having all variables defined at the same moment in time,

$$r_1 = r_0 + v_{1/2}\Delta t + \frac{1}{2}a_0(\Delta t)^2 \tag{2.11a}$$

$$v_1 = v_0 + \frac{1}{2}(a_0 + a_1)\Delta t \tag{2.11b}$$

where, given r_0, v_0, a_0, one would first calculate r_1, then the acceleration, and then v_1 using a predictor step $v_{1p} = v_0 + a_0\Delta t$ and then a correcting step $v_{1c} = v_{1p} + \frac{1}{2}(a_1 - a_0)\Delta t$.

At first glance, it might seem easy to develop a time-dependent timestep, merely changing the value of Δt depending on the needs of the system (smaller timesteps when particles are closely interacting, longer timesteps when only distant interactions are present), but this method can break down very quickly. The main problem is that it destroys time symmetry, which is important to the leapfrog method as it is a symplectic integrator, an integrator for which area conservation is important. When the timestep is changed, the leapfrog cannot accurately approximate the solutions of the differential equations and the truncation error is increased, so the scheme must be altered to accommodate a variable timestep.

The modified leapfrog scheme preserves time symmetry and does not directly impact the calculation of force (Hut et al., 1995). Written implicitly, it becomes

$$\xi_1 = f(\xi_0, \Delta t) \tag{2.12a}$$

$$\Delta t = \frac{1}{2}[h(\xi_0) + h(\xi_1)] \tag{2.12b}$$

where $\xi = (r, v)$ and the function f is equation (2.11) and h is the timestep criterion. It should be noted that despite the use of a_1 in the calculation of v_1 in equation (2.11a), that does not actually create an ξ_1 dependence in equation (2.12a), since a_1 may be determined directly from r_0 and v_0. These equations are then solved simultaneously at every time step for every particle. $h(\xi_0)$ is the timestep estimation function, which can be varied according to the application. An example of a timestep proportional to the free-fall times (Pelupessy et al., 2012) is, taking $\eta = 0.01$ as a constant:

$$\Delta t_{ij} = \eta \sqrt{\frac{r_{ij}}{a_{ij}}} \tag{2.13a}$$

$$\Delta t = \min_i \left(\frac{\Delta t_{ij}}{\left(1 - \frac{1}{2}\frac{\mathrm{d}\Delta t_{ij}}{\mathrm{d}t}\right)} \right) \tag{2.13b}$$

This method is originally a second-order scheme, which is not always sufficient for all applications with exceedingly long time or length scales. So there is a fourth-order generalization as well, where this modified leapfrog is attached to the Hermite algorithm (Makino, 1991) to create the scheme used in *hermite0*:

$$r_1 = r_0 + \frac{1}{2}(v_1 + v_0)\Delta t - \frac{1}{10}(a_1 - a_0)(\Delta t)^2 + \frac{1}{120}(j_1 - j_0)(\Delta t)^3 \tag{2.14a}$$

$$v_1 = v_0 + \frac{1}{2}(a_1 + a_0)\Delta t - \frac{1}{12}(j_1 - j_0)(\Delta t)^2 \tag{2.14b}$$

where $j = \mathrm{d}a/\mathrm{d}t$ is defined as the jerk and is calculated directly by differentiating the

acceleration. Using this instead of equation (2.11), the fourth-order scheme becomes

$$\xi_1 = g(\xi_0, \xi_1, \Delta t) \tag{2.15a}$$

$$\Delta t = \frac{1}{2}[h(\xi_0) + h(\xi_1)] \tag{2.15b}$$

In Figure 2.2, it can be seen that when using a time-symmetric variable timestep scheme, the build up of error over the same application and timescale is negligible when compared to a non-time-symmetric variable timestep scheme as described after equation (2.11).
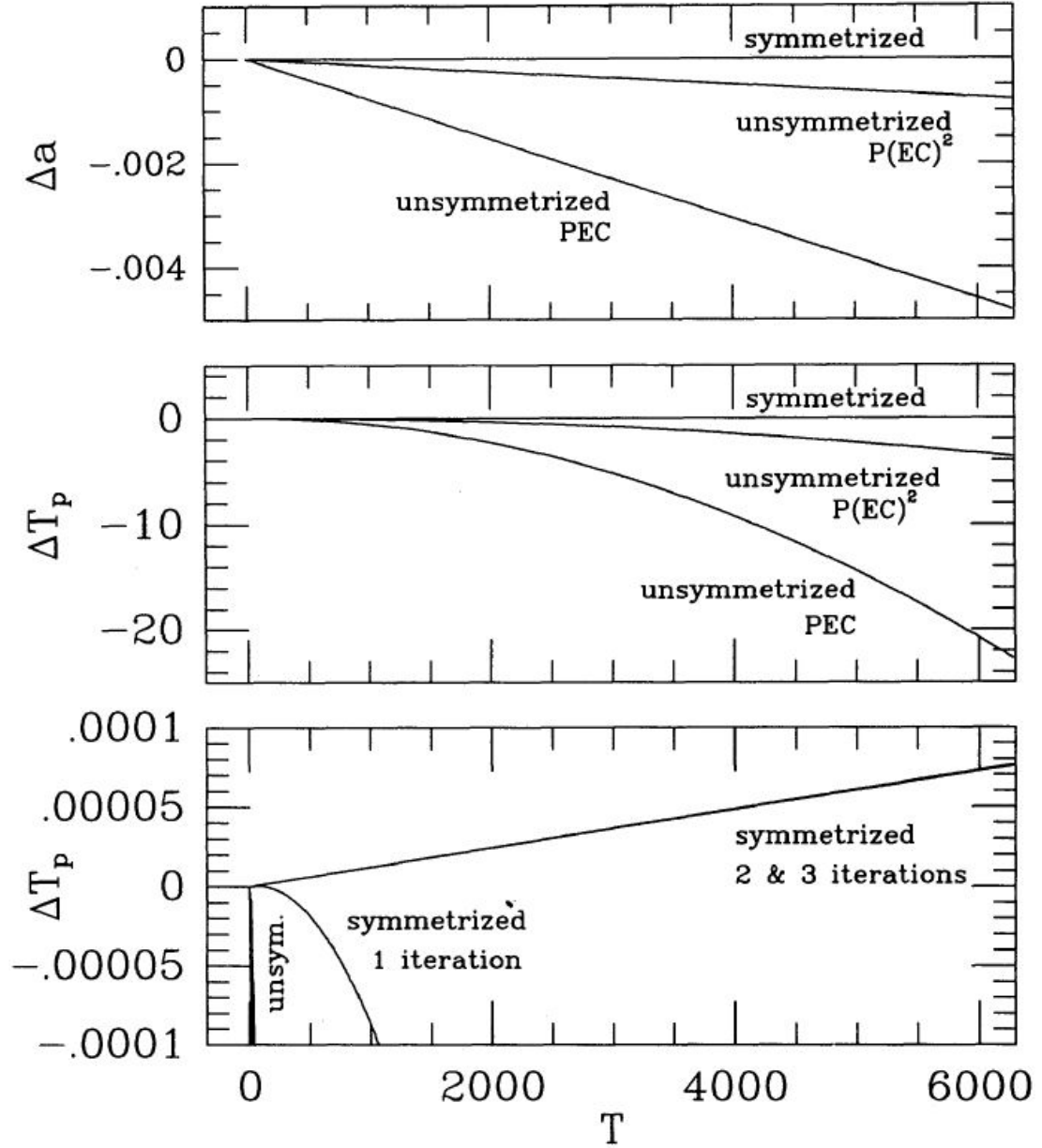
Figure 2.2: A comparison of errors for symmetrized and unsymmetrized integration of a Kepler ellipse. *Top*: The bottom line shows the drift in energy (through the stability of the orbit) when using the Predict Evaluate Correct (PEC) method of Hermite. The middle line shows the PEC method but with an additional force calculation at the end of every timestep, which provides some improvement. The top line shows the symmetrized scheme outlined in this section, which lead to an improvement of a factor of ≥ 16. *Middle*: The same three lines show the drift in the time of passage for the model. *Bottom*: An enlargement of the middle figure, showing how drastic the difference between the integration methods. (Hut et al. (1995), reproduced with permission)

2.3   Tree Codes

As we saw earlier, in order to determine a single star's trajectory while travelling through an N-body star system, one must calculate its gravitational encounters with every star it encounters (which includes every other star in the system). This can be a costly computation for a code, requiring $O(N^2)$ operations, an unattractive value with high N.

To overcome this computational limit, in the 1980's (Appel, 1985; Porter, 1985), hierarchical schemes were developed that relied on the fact that a particle interacts most strongly with its closest neighbours, and so less detailed information is needed for the more distant interactions. An ideal way would be to calculate each of the nearest neighbours individually, then group together sections of the more distant particles for less calculation. These schemes promised $N \log N$ scaling for their computational time, however their lists of interactions and data structures would become too complicated and tangled over time as complicated measures were needed to reconnect the groups of nearest neighbours at every timestep, which destroyed the timescaling. Also, the tree itself would become more of an arbitrary structure as time went on and particles changes positions, and so the errors would compound or be impossible to calculate.

2.3.1   Barnes-Hut Tree

In 1986, (Barnes and Hut, 1986) developed a scheme that overcame this tangling problem by rebuilding the tree from scratch at every timestep, allowing the nearest neighbours and groupings to be re-evaluated every time. This allowed the $N \log N$ scaling to be rigorously proven to be true.

Take an N-body system where the particles are randomly distributed throughout a cube volume called the 'root cell'. In a method known as *oct-tree*, the Barnes-Hut tree code (BH Tree) divides the 3D space into eight cells along the halfway point of each axis. Then, if a box contains more than one particle, it is called a 'twig' node and once again divided into eight cells. This process continues until every particle is in its own cell, called 'leaf' nodes. The process is illustrated in Figure 2.3. This does not actually divide the space into a grid, but is used to keep track of how the particles are related to one another, as in Figure 2.4.

This is the current method of dividing the cells. In their original paper (Barnes and Hut, 1986), they actually placed the particles one by one into the root cell. Every time a new particle was introduced, if it was placed into a cell with an existing particle, the cell would divide into eight cells. This was modified for numerical reasons, as the newer method allows for the tree to calculate force contributions at the same time, as opposed to having to do so in a separate process (Hernquist, 1988).

It can be useful to estimate how many divisions will be necessary to go from the root cell to a leaf node. This can be estimated using the average cell size containing
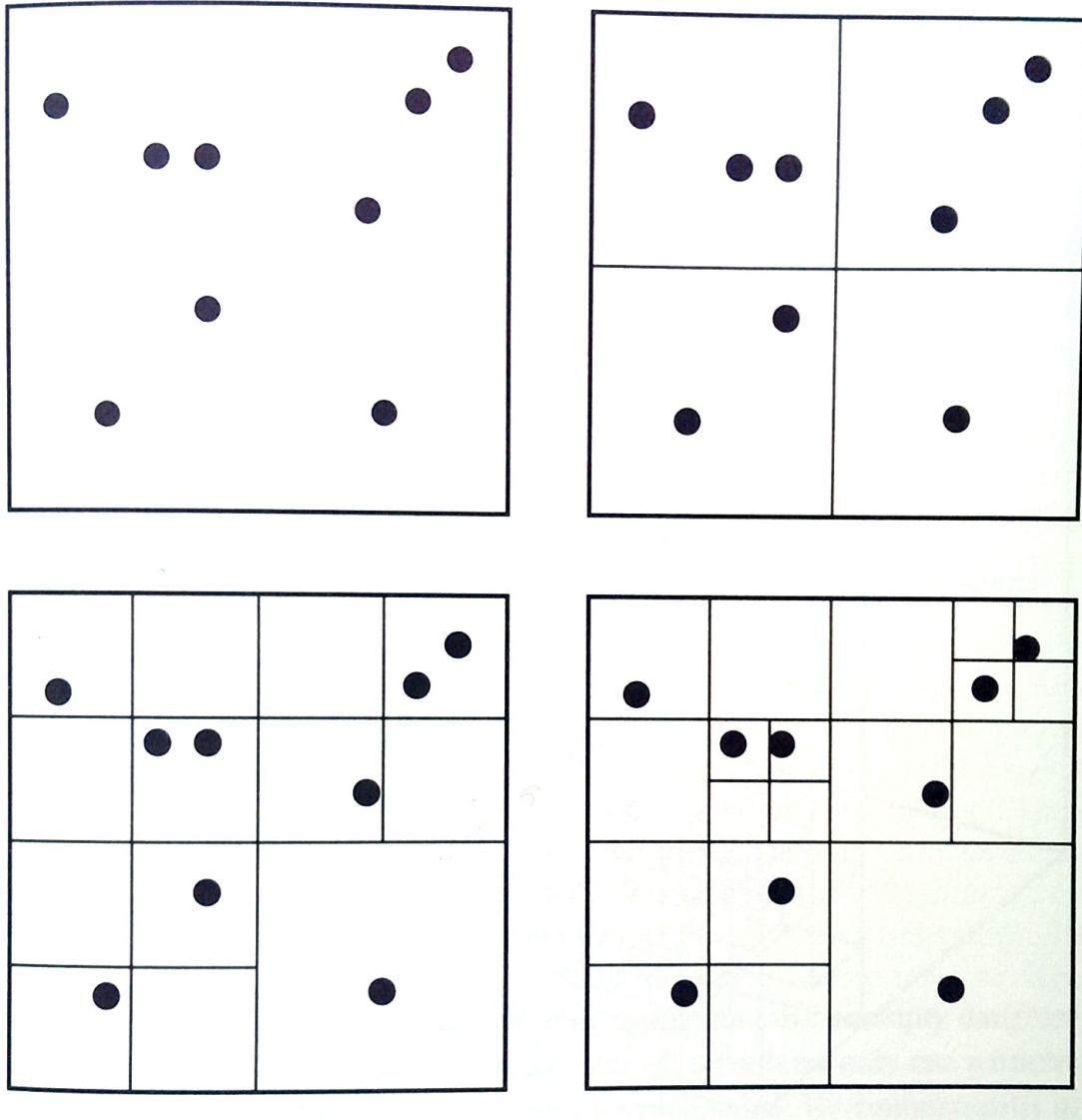
Figure 2.3: A 2D representation of the division of the root cell after particles are added. (Pfalzner and Gibbon (1996), reprinted with the permission of Cambridge University Press.)

one or more particles. If the total volume of the root cell is V, then the average volume of a particle-containing cell would be V/N and the average length of the cell would be $V^{1/3}/2$. This gives us,

$$\left(\frac{1}{N}\right)^{1/3} = \left(\frac{1}{2}\right)^{x} \tag{2.16}$$

where x is the number of divisions necessary. This can easily be solved,

$$x = \log_2 N^{1/3} = \frac{1}{2\log 2}\log N \simeq \log N \tag{2.17}$$

This means that it takes approximately $O(\log N)$ divisions to reach a certain leaf, and since there exist N particles, it would require $O(N \log N)$ calculations to construct the tree, as promised.

During this process, properties of each leaf are stored using an identifier, which leads to the position, mass, etc. in a data structure. Upon construction, each twig node will also store properties like centre of mass, total mass, and other things needed for force calculations. The total mass is simply calculated by

$$m_{parent} = \sum_i m_i(daughters) \tag{2.18}$$

And the centre of mass of the node,

$$\mathbf{r}_{parent} = \frac{\sum_i m_i \mathbf{r}_i}{\sum_i m_i} \tag{2.19}$$

This concludes the main construction of the tree, which takes $O(\log N)$ time and is repeated at every timestep to keep the data structures updated and untangled. The tree is now used in calculating the force, which also requires computational time of $O(\log N)$. For the closer particles, the force will be calculated directly, while for more distant particles, the force will be calculated for larger cells which would contain multiple particles.

To begin, we must first determine what constitutes a nearest neighbour and what constitutes a distant particle to be grouped in a larger cell. Barnes and Hut (1986) developed the 's/d' criterion, which still holds well against more modern alternatives such as Multipole Acceptability criterion (Salmon et al., 1994). In this method, for each particle, the size of a node s is compared to the distance from the particle d which is calculated by using the centre of mass for the node. If the condition

$$s/d \leq \theta \tag{2.20}$$

is met, where θ is some fixed tolerance parameter, then the force contribution of the node (no matter how many particles it contains) is added to the particle. If the condition is not met, then the node is divided into its daughter cells and the process continues until the condition is met or a leaf is encountered.

The use of different values for θ can greatly change both the accuracy and computation time for the force calculations. If $\theta = 0$, then it is equivalent to individually calculating every particle interaction and defeats the purpose of the hierarchical tree, and would in fact be longer than direct calculation as time would be wasted on the con-

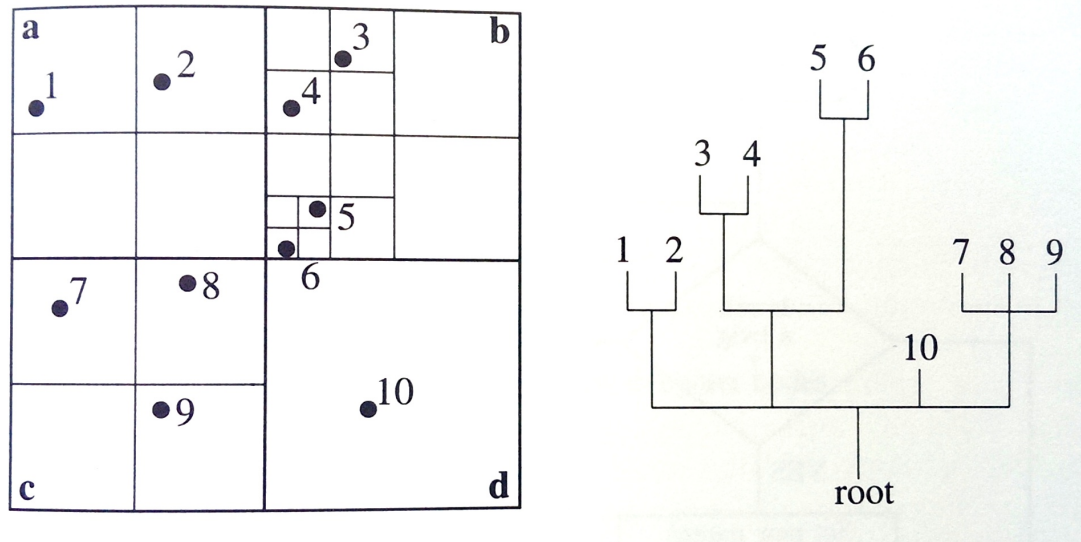Figure 2.4: The relationship between the division of the root cell and the branching tree structure. (Pfalzner and Gibbon (1996), reprinted with the permission of Cambridge University Press.)
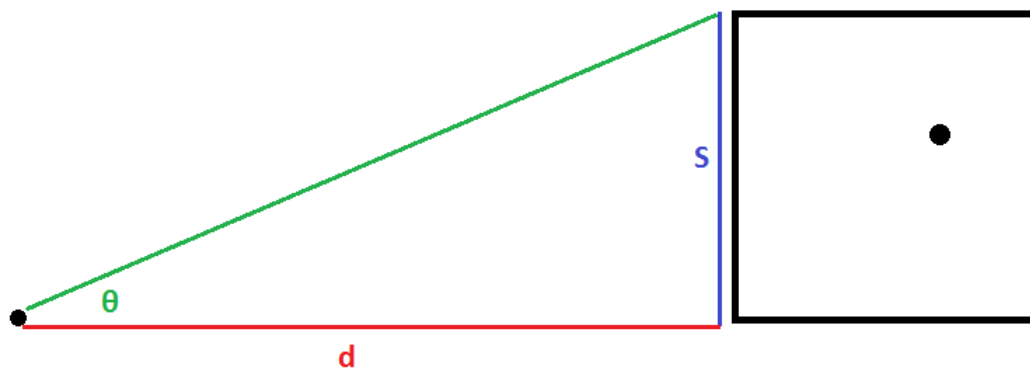
Figure 2.5: A 2D representation of the 's/d' criterion, where the particle is on the left and the node in question is on the right.

struction of the tree. The other extreme, taking $\theta \to \infty$, would lead to an inaccurate model, with interactions only occurring between particles and large pseudo-particles, even at very close distances. In most cases, choosing a θ between 0.1 and 1.0 is a reasonable choice (Barnes and Hut, 1986).

If θ is a nonzero number, than the time needed to complete the force calculations this way on a single particle is $O(\log N)$, and with N particles, the total time required is $O(N \log N)$ (Hernquist, 1988).

While tree codes are remarkably efficient, they do introduce approximations, especially for more distant particles. If a user desires the highest accuracy at the expense of computational time, the direct n-body method is still preferable, as it does not introduce any approximations into the solution for the equations of motion (though adaptive timesteps are often used, as they both limit errors and reduce computational time as discussed in Section 2.2.1).

2.4   Smoothed Particle Hydrodynamics

Smoothed Particle Hydrodynamics (SPH) was developed to simulate fluid flows in a way that was robust and accurate. It does this by using an interpolation method that can express a function as its values on a set of points or particles (Lucy, 1977). It is not mesh or grid based, but instead a Lagrangian method in that the coordinates move with the particles themselves and the mass is discretized (Monaghan, 1992).

The particles have a distance over which their properties are 'smoothed', termed

the *smoothing length* or h. What this means physically is that all the particle's relevant information and properties are included within that kernel. To begin, it is easiest to assume that the kernel is Gaussian in one dimension when trying to physically analyze a function, but many different kernels have been created (Gingold and Monaghan, 1982).

The integral interpolant for a function $A(\mathbf{r})$ is as follows

$$A_I(\mathbf{r}) = \int A(\mathbf{r}')W(\mathbf{r} - \mathbf{r}', h)\mathbf{dr}' \tag{2.21}$$

where W is a kernel function with the two properties

$$\int W(\mathbf{r} - \mathbf{r}', h)\mathbf{dr}' = 1 \tag{2.22a}$$

$$\lim_{n \to 0} W(\mathbf{r} - \mathbf{r}', h) = \delta(\mathbf{r} - \mathbf{r}') \tag{2.22b}$$

This interpolant can be approximated with

$$A_S(\mathbf{r}) = \sum_b m_b \frac{A_b}{p_b} W(|\mathbf{r} - \mathbf{r}_b|, h) \tag{2.23}$$

where for the particle b, $\mathbf{r}_b$ is the position, m_b is the mass, and ρ_b is the density.

For example, the density function can be written as

$$\rho_a(\mathbf{r}) = \sum_b m_b \frac{\rho_b}{\rho_b} W(|\mathbf{r} - \mathbf{r}_b|, h) = \sum_b m_b W(|\mathbf{r} - \mathbf{r}_b|, h) \tag{2.24}$$

which allows the density function of the system to be estimated just by using the masses and positions of the particles. Another example (Springel, 2010) is finding the local velocity divergence:

$$\nabla \cdot \mathbf{v} = \sum_b m_b \mathbf{v}_b \cdot \nabla W(|\mathbf{r} - \mathbf{r}_b|, h) \tag{2.25}$$

However a more accurate estimate may be taken by using the identity $\rho(\nabla \cdot \mathbf{v}) = [\nabla \cdot (\rho \mathbf{v}) - \mathbf{v} \cdot \nabla \rho]$ and then computing the kernel for both parts of the right-hand side and then calculating their difference, giving:

$$\rho_a(\nabla \cdot \mathbf{v})_a = \sum_b (\mathbf{v}_b - \mathbf{v}_a) \cdot \nabla_a W(|\mathbf{r}_a - \mathbf{r}_b|, h) \tag{2.26}$$

which also has the advantage of going to zero when all particles have the same velocity.

Moving forward, the particular kernel of interest is the kernel based on spline functions (Monaghan and Lattanzio, 1985).

$$W(\mathbf{r}, h) = \frac{\sigma}{h^\nu} \begin{cases} 1 - \frac{3}{2}q^2 + \frac{3}{4}q^3 & : 0 \leqslant q < 1, \\ \frac{1}{4}(2 - q)^3 & : 1 \leqslant q < 2, \\ 0 & : \text{otherwise} \end{cases} \tag{2.27}$$

where ν is the number of dimensions and σ is the normalization constant that changes with dimension, giving $\frac{2}{3}$, $\frac{10}{7\pi}$ and $\frac{1}{\pi}$.

The advantages of this particular kernel (which is used in GADGET-2, discussed in the next section) are that it has compact support, which means that it equals zero

when $r > 2h$ and so only covers a finite volume and thus the particle only interacts with the closest of its neighbours; and its second derivative is continuous, which means that the particle disorder is limited and so the errors from approximations can be kept low.

In addition,quantities such as momentum (linear and angular) and total energy are conserved. It is also possible to have adaptive smoothing lengths, where in dense regions, h decreases to create high resolution, and then in low-density regions, h increases to optimize the coverage.

2.4.1 GADGET-2

GADGET-2 is a cosmological simulation code that uses both the previously discussed SPH code to calculate the gas dynamics and tree code to compute the gravitational forces (Springel, 2005). Though the code was designed for large cosmological simulations, it also can be used for models of isolated systems, especially when used in conjunction with a direct summation code that calculates the gravitational dynamics of the stars in a smaller system (in our case, *hermite0*) while the SPH portion of GADGET-2 models the hydrodynamics of the gas and an integrator like Bridge (discussed in Section 2.4) allows the two parts to communicate. While GADGET-2 can model both stars and gas at the same time, in a smaller, isolated system, it is more ideal to model the parts separately with different processes in parallel.

The gas is modeled using collisionless dynamics that can be described using the

Hamiltonian

$$H = \sum_i \frac{\mathbf{p}_i^2}{2m_i a(t)^2} + \frac{1}{2} \sum_{ij} \frac{m_i m_j \varphi(\mathbf{x}_i - \mathbf{x}_j)}{at} \qquad (2.28)$$

where $H = H(\mathbf{p}_1, ..., \mathbf{p}_N, \mathbf{x}_1, ..., \mathbf{x}_N, t)$. In this equation, $\mathbf{x}_i$ are coordinate vectors, and $\mathbf{p}_i = a^2 m_i \dot{\mathbf{x}}_i$ are the canonical momenta. $\varphi(\mathbf{x})$ is the interaction potential, where G is the gravitational constant and ρ is the local density, and gives us Poisson's equation:

$$\nabla^2 \varphi(\mathbf{x}) = 4\pi G \rho(\mathbf{x}) \qquad (2.29)$$

The spline function as described in the previous section is also used with some numerical changes,

$$W(\mathbf{r}, h) = \frac{8}{\pi h^3} \begin{cases} 1 - 6\left(\dfrac{r}{h}\right)^2 + 6\left(\dfrac{r}{h}\right)^3 & : 0 \leqslant \dfrac{r}{h} < \dfrac{1}{2}, \\[2ex] 2\left(1 - \dfrac{r}{h}\right)^3 & : \dfrac{1}{2} \leqslant \dfrac{r}{h} < 1, \\[2ex] 0 & : \dfrac{r}{h} > 1. \end{cases} \qquad (2.30)$$

Note that in this case, the kernel goes to zero at h, as opposed to the more typical $2h$. This was done for consistency with previous work and has no consequence on the results.

For the hydrodynamics, the formulation of SPH used in GADGET-2 conserves both energy and entropy, regardless of using fixed or adaptive smoothing lengths.

The adaptive smoothing lengths h_i are defined as to always contain a fixed mass

$$\frac{4\pi}{3}h_i^3\rho_i = N_{sph}\bar{m} \tag{2.31}$$

where N_{sph} is the typical number of nearest smoothing neighbours and $\bar{m}$ is the average mass of a particle, which is not necessarily a constant, though the total mass contained within the smoothing length is constant.

This gives the equations of motions for the particles

$$\frac{dv_i}{dt} = -\sum_{j=1}^{N} m_j \left[f_i \frac{P_i}{\rho_i^2} \nabla_i W(|\mathbf{r}_i - \mathbf{r}_j|, h_i) + f_j \frac{P_j}{\rho_j^2} \nabla_i W(|\mathbf{r}_i - \mathbf{r}_j|, h_j) \right] \tag{2.32}$$

where the coefficients are

$$f_i = \left(1 + \frac{h_i}{3\rho_i} \frac{\partial \rho_i}{\partial h_i} \right)^{-1} \tag{2.33}$$

and the particle pressures are $P_i = A_i \rho_i^\gamma$ where A is entropy and γ is the adiabatic index or ratio of specific heats (Springel and Hernquist, 2002). This completely describes the fluid dynamics of a system, provided that it does not experience any shocks or external sources of heat.

To properly model any shocks experienced, the system needs an artificial viscosity, which uses a viscous force:

$$\left. \frac{dv_i}{dt} \right|_{visc} = -\sum_{j=1}^{N} m_j \Pi_{ij} \nabla_i \bar{W}_{ij} \tag{2.34}$$

where $\Pi_{ij} \geq 0$ is only non-zero when particles approach each other in physical space. We can define an equation for the viscosity:

$$\Pi_{ij} = -\frac{\alpha}{2} \frac{(c_i + c_j - 3w_{ij})w_{ij}}{\rho_{ij}} \qquad (2.35)$$

where α is a parameter that modifies the strength of the viscosity, c_i is the speed of sound for a particle, $w_{ij} = \mathbf{v}_{ij} \cdot \mathbf{r}_{ij}/|\mathbf{r}_{ij}|$ the relative velocity of two particles projected onto their separation vector, and ρ_{ij} is the mean density (Monaghan, 1997). The artificial viscosity of a single particle is dependent on the relative velocities of the surrounding particles and is meant to keep adjacent particles from getting too close to one another (Johnson, 1996). In the equations of motion, the viscosity acts like an excess pressure, $P \simeq (1/2)\rho_{ij}^2\Pi_{ij}$ on the particles.

2.5   Bridge

When an system is being modelled that includes one component that needs short timesteps for high accuracy and another component that needs longer timesteps due to a large number of particles, communicating between those components and treating the system as a whole can be difficult. To help solve this, Fujii et al. (2007) developed the Bridge scheme (Realistic Interactions in Dense Galactic Environments), a direct-tree hybrid N-body algorithm.

In the Bridge scheme, the interactions within a star cluster are calculated using a direct and Hermite scheme, leading to high accuracy and short timesteps. The

interactions between the cluster and its environment (be that the galaxy as a whole or gas clouds) are calculated using a tree algorithm as described in section 2.2. In order to combine these two approaches, Bridge uses a modified version of the Mixed Variable Sympletic (MVS) method (Wisdom and Holman, 1991), which was originally used to model long-term planetary interactions.

In the new hybrid method, the Hamiltonian of the system is split into two parts: H_α, the potential energy for all gas-gas particle or gas-cluster particle gravitational interactions; and H_β, the total kinetic energy and the potential energy for cluster-cluster particle gravitational interactions.

$$H = H_\alpha + H_\beta \tag{2.36a}$$

$$H_\alpha = -\sum_{i<j}^{N_G} \frac{Gm_{G,i}m_{G,j}}{r_{ij}} - \sum_{i=1}^{N_G}\sum_{j=1}^{N_{SC}} \frac{Gm_{G,i}m_{SC,j}}{r_{ij}} \tag{2.36b}$$

$$H_\beta = -\sum_{i=1}^{N_G} \frac{p_{G,i}^2}{2m_{G,i}} + \sum_{i=1}^{N_{SC}} \frac{p_{SC,i}^2}{2m_{SC,i}} - \sum_{i<j}^{N_{SC}} \frac{Gm_{SC,i}m_{SC,j}}{r_{ij}} \tag{2.36c}$$

where N_G is the number of particles in the gas and N_{SC} is the number of particles in the star cluster.

Looking at

$$\frac{df}{dt} = \{f, H\} \tag{2.37}$$

we can define differential operators α and β as $\alpha f := \{f, H_\alpha\}$ to get the solution

$$f(t) = e^{t\alpha} f(0) \tag{2.38}$$

Using the Hamiltonian in equation (2.36) with the MVS algorithm, we then get for the time evolution,

$$f'(t + \Delta t) = e^{\frac{1}{2}\Delta t\alpha} e^{\Delta t\beta} e^{\frac{1}{2}\Delta t\alpha} f(t) \tag{2.39}$$

Since this Hamiltonian cannot be solved analytically (unlike the original MVS, which used analytically solvable Keplerian motion), higher-order integrators must instead be used. For the star cluster particle interactions, a Hermite scheme is used, where the subscripts 0, $\frac{1}{2}$ and 1 indicate fractions of timesteps (i.e. t, $t + \frac{1}{2}\Delta t$ and $t + \Delta t$), and $\mathbf{a}_{\{G \to SC, 0\}}$ represents the acceleration from the gravitational interactions of all gas particles on the star cluster particles.

$$\mathbf{v}'_{SC,0} = \mathbf{v}_{SC,0} + \frac{1}{2}\Delta t\, \mathbf{a}_{\{G \to SC, 0\}} \tag{2.40a}$$

$$\mathbf{x}_{SC,0} \to (\text{Hermite Scheme}) \to \mathbf{x}_{SC,1} \tag{2.40b}$$

$$\mathbf{v}'_{SC,0} \to (\text{Hermite Scheme}) \to \mathbf{v}'_{SC,1} \tag{2.40c}$$

$$\mathbf{v}_{SC,0} = \mathbf{v}'_{SC} + \frac{1}{2}\Delta t\, \mathbf{a}_{\{G \to SC, 1\}} \tag{2.40d}$$

For the gas particle interactions, a more simplistic leapfrog method is used, which lacks the high accuracy but is a much faster integrator, which is preferable for the

much larger number of particles within this component. In the following, $\mathbf{a}_{\{All \to G,0\}}$ represents the acceleration from the gravitational interactions of all the particles in the system on the gas particles.

$$\mathbf{v}_{G,\frac{1}{2}} = \mathbf{v}_{G,0} + \frac{1}{2}\Delta t \ \mathbf{a}_{\{All \to G,0\}} \tag{2.41a}$$

$$\mathbf{x}_{G,1} = \mathbf{x}_{G,0} + \Delta t \ \mathbf{v}_{G,\frac{1}{2}} \tag{2.41b}$$

$$\mathbf{v}_{G,1} = \mathbf{v}_{G,\frac{1}{2}} + \frac{1}{2}\Delta t \ \mathbf{a}_{\{All \to G,1\}} \tag{2.41c}$$

These separate methods are then combined with a tree at certain intervals to create the Bridge scheme. At time t_0, a tree is constructed to calculate $\mathbf{a}_{\{G \to SC,0\}}$ and $\mathbf{a}_{\{All \to G,0\}}$. In the construction of the tree, two masses were given at every node, one for gas particle masses and one for total mass. This allows for one tree to be used in calculating all the accelerations. Then the velocities of both the star cluster and gas are given a 'kick' using equations (2.40a) and (2.41a) respectively. The positions and velocities of the star cluster are then updated using the Hermite scheme (equations (2.40b) and (2.40c)) while the gas determines the positions using equation (2.41b). Another tree is then constructed at $t_{\frac{1}{2}}$ to once again calculate the accelerations $\mathbf{a}_{\{G \to SC,1\}}$ and $\mathbf{a}_{\{All \to G,1\}}$. Finally, both the star cluster and gas velocities are given another kick using equations (2.40d) and (2.41c) to their final velocity for the total timestep.

2.6   AMUSE

When running an astrophysical simulation, one often needs to use more than one code to properly model the system's components, but these codes were each designed with a main problem in mind and so do not necessarily cooperate with each other or sometimes even work outside their native domain. So the open-source Astrophysical Multi-purpose Software Environment (AMUSE) was developed to provide a single interface and simple access to multiple established codes, allowing for simulations that use many different types of physics at once (Pelupessy et al., 2013).

As can be seen in Figure 2.6, the framework of AMUSE consists of three main parts: the Python *user script*, the Python and C/Fortran *interface*, and the C/C++/ Fortran *community code* base. The user script is written directly by the user, and indicates the initial conditions, which codes to use, and possibly data analysis such as Matplotlib or Gnuplot. The interface layer then takes this information and communicates it (as well as units and an abstract data model) in the proper way to the community code, which runs the actual physics involved.

The interface of a community code essentially imports the code as a remote library using a remote function call protocol based on Message Passing Interface (MPI). This allows for a built-in parallelism and separation of memory space. The benefits of built-in parallelism over parallelism being added later is that it is possible for features added to the code at later dates to destroy the artificial parallelism. The separation of memory space is incredibly useful because without the MPI, having multiple community codes all using the same memory reservoir made it nearly impossible to initiate
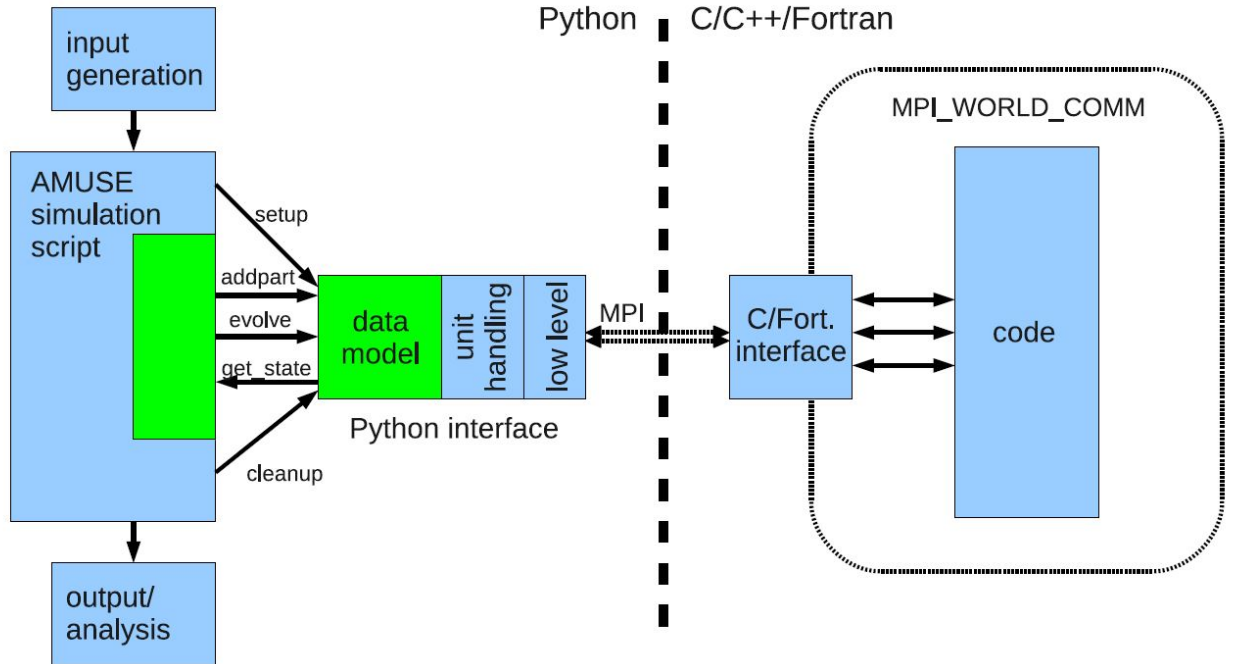
Figure 2.6: Framework of AMUSE. On the left side is the user script (``AMUSE simulation script″) and the interface, with arrows showing the direction of information flow. On the right side is the community code (``code″) as well as its interface that connects to the Python code using MPI. This shows how the interface is not a single script, but an amalgamation of different modules that communicate between the user script and the community code. (Pelupessy et al. (2013), reproduced with permission ESO.)

more than one code at a time. Using MPI turns each of the community codes into its own executable, allowing it to take up its own memory space, and so the global memory problem disappears.

A drawback of this interface method is that since there is no global memory reservoir, it is not as straightforward to share simulation data between multiple codes. This means that the interface must be carefully designed so that all the proper information can be passed between codes, but not too much data as would slow down the process too much. Although, even in the simple direct-link scenario, connecting a C and a Fortran code has its own problems (using multiple *f2c* (a program for converting Fortran 77 to C), *f2py* (a Python package for converting Fortran 77/90/95 to Python) or *SWIG* (a tool for converting C into various computing languages) codes to translate between languages) that still make the MPI scheme more appropriate.

When one community code or more is initiated, the interface is started separately and waits for a message from the user script. It then relays this information to the proper community code, executes the required subroutine and sends back any results. The community code continues to run its loops until told to stop.

Another important part of AMUSE is its ability to keep track of different *unit systems* within the same simulation. It forces the user to identify exactly which system of units to use for all the quantities and has several converters to change between different systems. This allows for the interface to automatically convert all the data into the proper system for each community code and then convert back for the results. It also allows for codes that have under-specific units (i.e. N-body codes

using G = 1) to be paired with unit-specific codes with little problem.

In order to simplify book-keeping, a specific kind of data model is also used, called *particle sets*. A particle is an object with multiple properties such as mass, position, velocity, etc., as well as an identification number. The data of a particle set is kept in the Python memory space of the interface and are then copied directly into the community codes upon initiation. These sets can then be updated by synchronizing the Python memory set with the community code set though the use of a defined channel.

A common problem when running multiple codes is the differing work-flows (not timesteps, but the process in which the code evolves the model). For example, a gravitational dynamics code needs to add and remove particles and track these changes for its calculations. However, a tree code needs to reconstruct its entire tree before any gravitational forces can be calculated. It would be inefficient to ask the dynamics code to rebuild the tree every time a particle is added or to ask the tree code to update with an add-particle method each time. The solution AMUSE uses is to flag the state of the code and then only update the tree once all particles have been added or removed. It keeps track of the state each code is in and only allowing access to the code and data when possible, therefore minimizing both errors and wasted computational time. In practice, codes of a similar type (i.e. all gravitational codes) have a similar work-flow, so there is little trouble in pairing them. However, when codes of different types are paired, like a gravitational code with an SPH code, a more complex approach is needed. AMUSE uses the Bridge integrator discussed in the previous section to evolve the model while taking into account the differing timesteps

of the two codes.

AMUSE includes several modules that make setting up the initial conditions of systems very simple such as N-body particle generators (Plummer and King models) and initial mass functions (Salpeter, Scalo and Kroupa).

The Plummer model is a density law developed to describe observations of globular clusters (Plummer, 1911), where using M as the total mass of the cluster, a as the Plummer radius (a scaling parameter that identifies the radius of the cluster core, where the surface density drops to half its central value, through the relation $r_c = a\sqrt{\sqrt{2}-1}$), the density profile is given by:

$$\rho(r) = \left(\frac{3M}{4\pi a^3}\right)\left(1+\frac{r^2}{a^2}\right)^{\frac{5}{2}} \tag{2.42}$$

and, using G as the gravitational constant, the potential is given by:

$$\Phi(r) = -\frac{GM}{\sqrt{r^2+a^2}} \tag{2.43}$$

An initial mass function (IMF) describes the distribution of masses in a population of stars. It is usually given as a series of power laws, which give the number of stars $\xi(m)dm$ that have a mass within a certain range $m+\Delta m$ is proportional to $m^{-\alpha}$, where α is a dimensionless constant. In the Salpeter IMF (Salpeter, 1955), an $\alpha = 2.35$ is taken, to give a function of:

$$\xi(m)dm = \xi_0\left(\frac{m}{M_{sun}}^{-2.35}\left(\frac{\Delta m}{M_{sun}}\right)\right) \tag{2.44}$$

2.7   Summary

In this chapter, we have outlined the basics of stellar dynamics, in particular, we have discussed various timescales and their effect on dynamical systems, as well as equipartition of energy and core collapse. We looked at *hermite0* and how its scheme is a faster and more accurate modification of the well known leap-frog method. We have also discussed tree codes and SPH codes as well as the specific codes used in this research. Tree codes are an evolution of direct N-body codes, designed to shorten the amount of computing time necessary to calculate the gravitational forces without losing accuracy. *BHTree* does this by constructing an oct-tree at every timestep to identify nearest neighbours and further particles whose contributions can be approximated as a group. SPH codes were developed to simulate fluids using an interpolation method. It uses particles whose properties are included within a defined kernel. *GADGET-2* is an SPH code that uses the spline kernel and an adaptive smoothing length in modeling gas dynamics. We have also looked at how the *Bridge* integrator works to combine a gravitational dynamics code with an SPH code in a computationally efficient manner. We have outlined the framework of *AMUSE* and how it can implement multiple established codes at once, even ones written in different computing languages, in a single simulation without much inconvenience to the user.

Chapter 3

Method and Results

3.1 Introduction

In this chapter, we will present the details of the simulations we ran to investigate how these young embedded clusters evolve, with their high ellipticity and large fraction of gas mass; if the lack of older elliptical clusters is due to evolution or dissipation of the young clusters; and how the presence of this gas affects the clusters, and how this might affect how we look at gas expulsion.

3.2   Model Initial Conditions

In this thesis, we present the results of 6 models of small star clusters embedded in their molecular gas cloud. The properties of each model are given in Table 3.1.

Table 3.1: Initial Conditions

Model	e	Stellar Mass	Gas Mass	f_{gas}	N_{star}	N_{gas}
A	0	$66M_\odot$	$66M_\odot$	50%	200	100K
B	0.66	$66M_\odot$	$66M_\odot$	50%	200	100K
C	0.87	$66M_\odot$	$66M_\odot$	50%	200	100K
D	0	$66M_\odot$	$200M_\odot$	75%	200	100K
E	0.66	$66M_\odot$	$200M_\odot$	75%	200	100K
F	0.87	$66M_\odot$	$200M_\odot$	75%	200	100K

We chose to base our cluster on a Plummer sphere, as it is a well known density profile used to describe observations of known clusters. We also used a Salpeter initial mass function to describe the distribution of masses in our population of stars. Although a Salpeter IMF could theoretically produce a massive star ($M > 100M_\odot$), such a star would have drastic effects on its surroundings due to its large mass as well as production of ionizing radiation, stellar wind, and jets and outflows. Such a massive star does not exist in the MYStIX data (Feigelson, 2010), so a maximum mass was introduced to the IMF of $m_{max} = 10M_\odot$. We chose a total star mass of $66M_\odot$, and kept the distribution of masses identical for every run. However, for the gas mass, we first defined the gas mass fraction as:

$$f_{gas} = \frac{M_{gas}}{M_{total}} \tag{3.1}$$

and also expressed this value as a percentage for ease of use. We varied this gas mass

fraction in a range $0.50 \leq f_{gas} \leq 0.75$, as we wanted to also investigate the effect of gas mass on the dynamics, since the observed clusters were embedded clusters with varying amounts of gas.

We used 200 star particles, to keep with the scale of MYStIX observations. Although many known open clusters have many more stars (on the order of 1000 stars), the young clusters in MYStIX are generally small and as the eventual purpose of this project is to simulate actual MYStIX clusters, it is more useful to create models of their approximate size to observe more general results. We used 100,000 gas particles because the evolution of this system took a reasonably short time without the use of a supercomputer and we were able to produce several simulations efficiently. We used an rscale of 0.5 pc, which gives a half-mass radius of 0.4 pc, to give similar cluster sizes as seen in the MYStIX data.

The positions and velocities of the stars were randomly calculated such that the kinetic and potential energies were 0.25 and -0.5 in N-body units (a unit system used for N-body simulations where the base units are chosen so that the gravitational constant, G, is normalized), respectively. This however can easily be modified to fit a velocity dispersion profile or accurate location data if needed. For the gas, the particles have an initial velocity of zero, so all its initial energy is potential. In later study, we are interested to investigate how giving the gas energy - through randomized velocity, rotational velocity, or as if the gas was along a filamentary structure - could affect the model. Having a non-zero velocity for the gas would likely change how the gas behaves, especially initially, as a non-zero velocity would prevent the gas from immediately in-falling toward the centre of the cluster.

Since the main parameter we wanted to investigate was the eccentricity of the cluster, we chose to look at $e = 0.0, 0.66, 0.87$. This provided us with a range of values that could be seen in the MYStIX data while also giving a large enough spread between values that the differences between them could easily be seen. This ellipticity was created by compressing the existing Plummer sphere for both the stars and gas particles along the desired axis. The cluster could be made spherical, oblate or prolate. For this thesis, we chose to create an oblate spheroid, where one axis (we chose the z axis) is shorter than the other two. The alternative is a prolate spheroid, with one axis longer than the other two. We believe that similar results would come from using a prolate spheroid, as the furthest ends of the longer axis are still only as far as the edge of the oblate equator, and would in fact experience more gravitational force toward the core, since the core would be more dense than any of the surrounding space (as opposed to the oblate spheroid, where the furthest edges have forces pulling them in more tangential directions due to its shape). To calculate the eccentricity of an ellipse (or, in three dimensions, a spheroid), one needs the lengths of the semi major axis (or equatorial axis for an oblate spheroid), a, and the length of the semi minor axis (or polar axis), c, where $a \geq c$:

$$e = \sqrt{1 - \frac{c^2}{a^2}} \qquad (3.2)$$

The various units were tracked and managed by AMUSE, with conversions between units occurring whenever a community code was invoked. A conversion function was created using the total mass of the system and the rscale length. This means that

the model had to be scaled properly, which was done using AMUSE's *scaletostandard* command. This allowed both the gas and star Plummer spheres to be combined into a single simulation.

Once the initial cluster was generated, we allowed it to evolve in AMUSE for 5 Myr. This was longer than the relaxation time of the stars, which is ~ 4 Myr, allowing for dynamical stability to possibly be achieved and for meaningful conclusions to be drawn. This time frame also allows for multiple gas crossing times, which is ~ 1.5 Myr, allowing the gas to interact and evolve even further than the stars, which was expected due to the difference in particle sizes between the stars and gas. From these timescales, we would expect the stars to change from their elliptical system at a much slower rate than the gas particles.

The data of both the stars and gas' properties was stored at every timestep of approximately 8000 years (this time varies with the gas fraction, as that changes the total mass of the system which has an effect on N-body time, the units with which the code counts time). From these data, a snapshot of both the gas density map and star positions was made every 0.25 Myr to observe the general movements of both the gas and stars.

We do not expect an event like core collapse to occur, as the timescale of the simulation is not long enough to truly allow the core to condense to this extent. We also do not have binary stars in this initial creation of the cluster, nor did any form during the course of the runs of our models, but the possibility does remain of binary systems forming of their own accord during the simulation time especially if

the models are allowed to run for longer periods of time.

3.3 Models

We consider six models with the varying parameters as shown in Table 3.1. We run each of the three eccentricities with two different gas mass fractions (and therefore two different total system masses). Of the most interest are the two models with the largest eccentricity, as these differ the most from any other dynamical study of embedded star clusters.

We then used the R package [1] developed by Kuhn et al. (2014) to determine the ellipticity of the cluster. The coordinates of the particles use meters or parsecs as units, easily convertible from one to the other. These, together with the distance from a similar MYStIX cluster as this model's initial parameters were loosely based on an existing MYStIX cluster DR-21, could be used to convert the cartesian coordinates of the model into RA and Dec coordinates to match the observational data. Feeding these new coordinates into the R package, we could output an ellipticity based on the stellar density. This ensures that we used the same method devised to determine ellipticities of the MYStIX project.

---

[1]R is a programming language and software environment specifically designed for statistical analysis and computing. Packages can be developed for specific projects and then easily imported into the environment. More information is available at www.r-project.org

3.4   Results

In this section, we present the results of the simulations described in Section 3.3. First we analyse the results of simulations with a gas mass fraction of 50%, then investigate the ramifications of a larger gas cloud by analysing the simulation with a gas mass fraction of 75%. Finally, we discuss how these results compare with the findings of the MYStIX project.

3.4.1   50% gas mass

In Figure 3.1, we have the snapshots taken of the XZ plane for the model with a gas mass fraction of 50% at various timesteps. The length and width of the snapshot is 3.0 parsec to have a view of most of the gas cloud. In these plots, the blue points are stars with $M < 0.9 M_\odot$, green points have $0.9\ M_\odot < M < 2.5 M_\odot$ and red points have $2.5 M_\odot < M < 10 M_\odot$. Also shown is the gas density plot in the copper colour scheme, with the log density displayed on the side in units of cm^{-3}.

In panel 3.1a), we have pictured the model in its initial state, as a modified Plummer density distribution. The stars and gas are in an elliptical shape with $e = 0.5$ and it can be seen that the gas is clumped by the randomized distribution. These clumps smooth out into a more continuous distribution within 100,000 years.

In panel 3.1b), we have the snapshot of the model at 0.75 Myr. The stars at the far edges of the ellipse can be seen moving closer to the centre of the cluster, following the gravitational pull of the centre of mass. Not every star follows this direct route

Figure 3.1: Snapshots of the XZ plane of the $f_{gas} = 0.50$ model at 0.0, 0.75, 1.75 and 2.75 Myr. Blue points are stars with $M < 0.9 M_\odot$, green points have $0.9\ M_\odot < M < 2.5 M_\odot$ and red points have $2.5 M_\odot < M < 10 M_\odot$. The pink oval shows the ellipticity of the core. Also shown is the gas density plot.
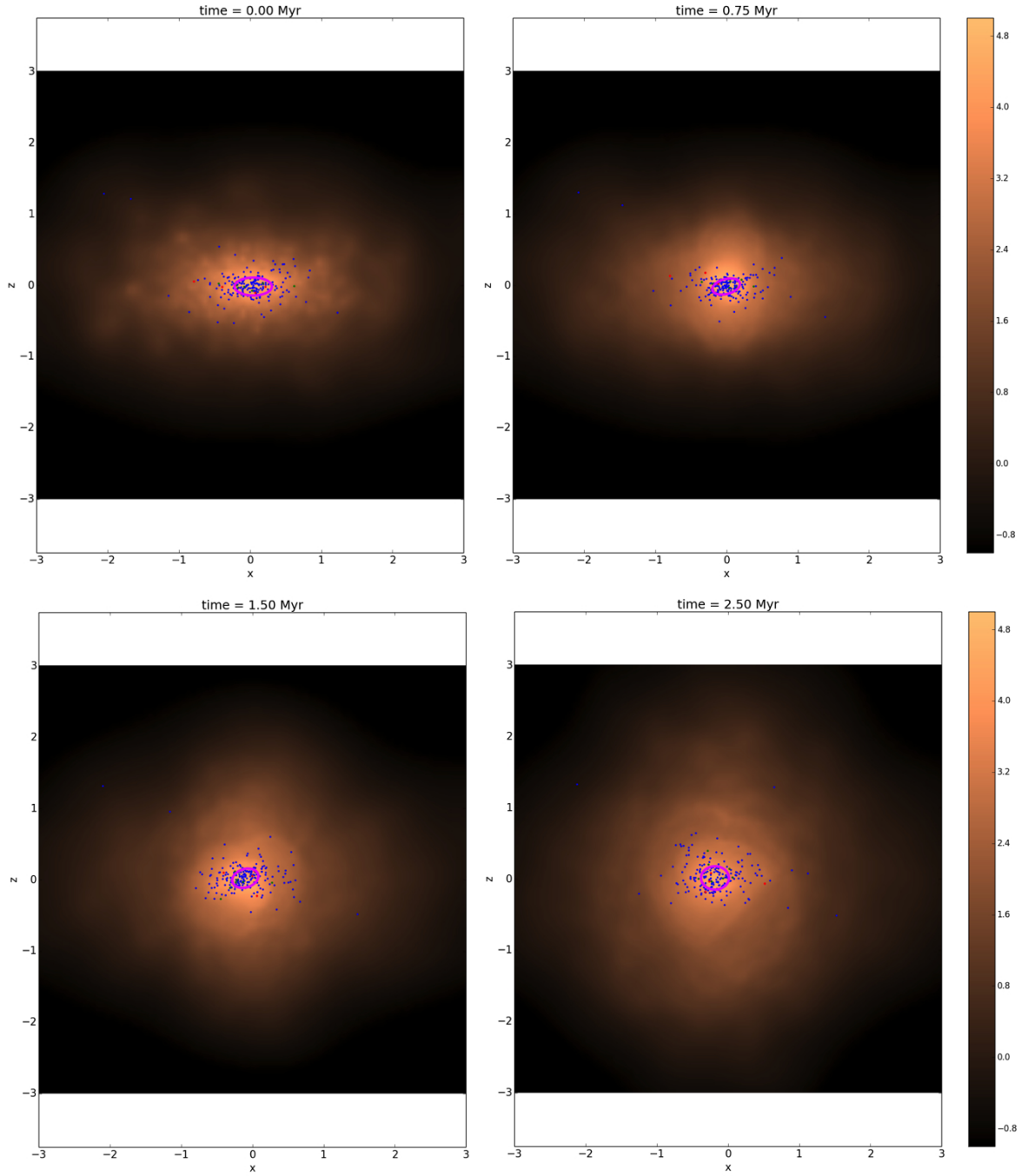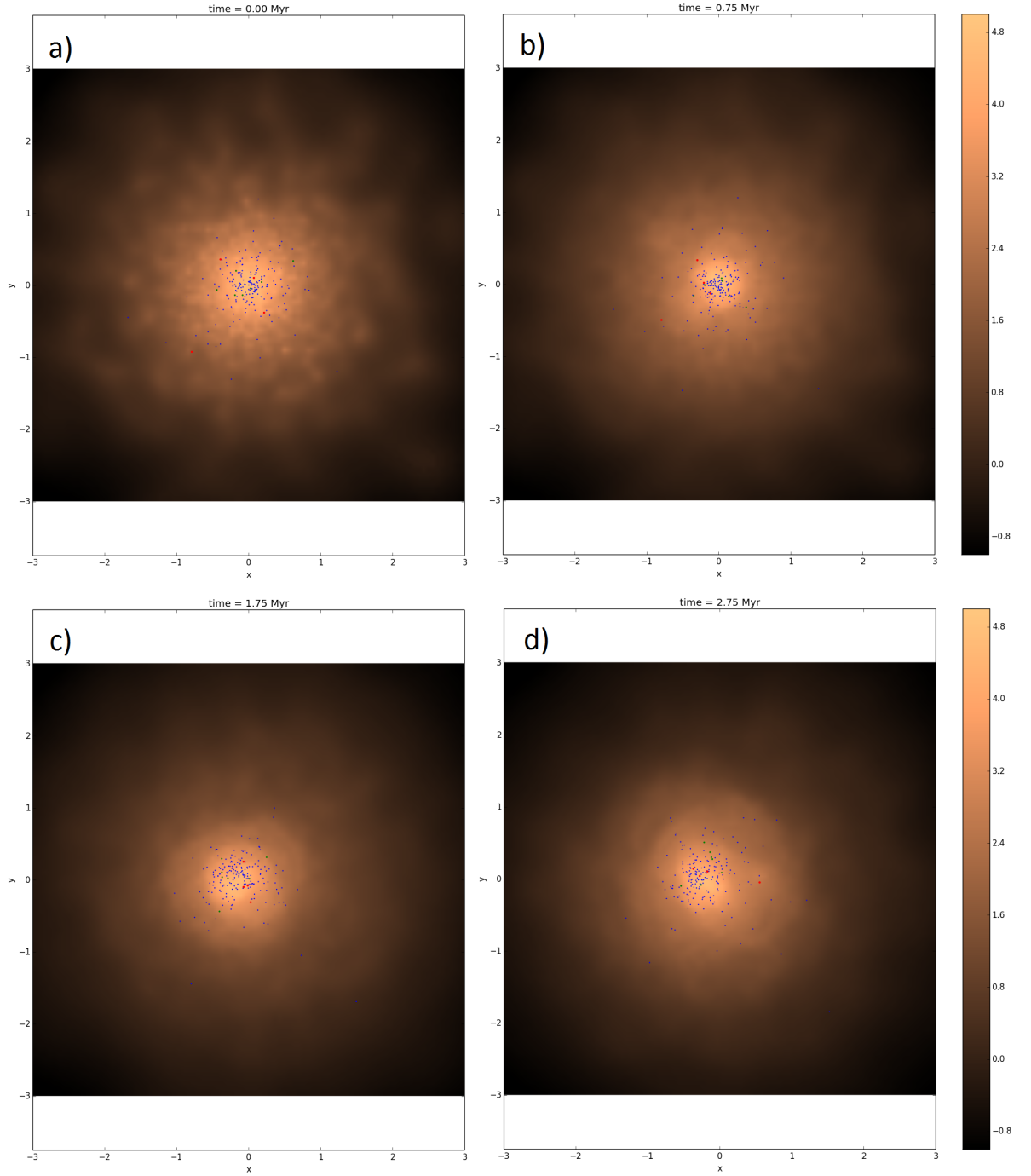
Figure 3.2: Snapshots of the XY plane of the $f_{gas} = 0.50$ model at 0.0, 0.75, 1.75 and 2.75 Myr. Blue points are stars with $M < 0.9 M_\odot$, green points have $0.9\ M_\odot < M < 2.5 M_\odot$ and red points have $2.5 M_\odot < M < 10 M_\odot$. Also shown is the gas density plot.

however, as they were also initially given a random velocity, as well as the effects of any interactions between two or more neighbouring stars (since gravitational force decreases with r^2, the effects of a nearby star, even a small one, can have a larger effect than a large mass at a large distance). Indeed, a small number of stars ($\sim 3\%$) were pushed away from the cluster and are now further from the core than they were initially.

We can also see how the gas is moving in a different way than the stars. Even though the mean velocity of the gas particles is lower than that of the star particles ($v_{gas} \approx 250$ m/s compared to $v_{stars} \approx 800$ m/s), the overall pattern and shape of the gas cloud seems to evolve at a faster rate. Already, at just 0.75 Myr, a mostly spherical central core of gas has formed with a radius of 0.25 pc. Like the stars, the gas at the furthest edges of the ellipse move inwards toward the core. However, there is an additional 'rebound' effect visible along the z axis on both sides of the central density sphere, where gas seems to be pushed out from the centre after moving in from the edges.

In panel 3.1c), we have the snapshot of the model at 1.75 Myr. The stars have slightly rebounded from the core of b), with the dense central stars remaining in place but the stars of the edge moving outwards in all directions. In this particular run, it can be seen that most of the larger stars ($M > 0.9 M_\odot$) have travelled to the core of the cluster, where initially they were scattered throughout the cluster. In Figure 3.3, we can see that the mass segregation of the stars in the cluster does increase as the model evolves. This is measured by calculating the Gini coefficient (Converse and Stahler, 2008), which is related to the cumulative fractional number f_N (fraction of
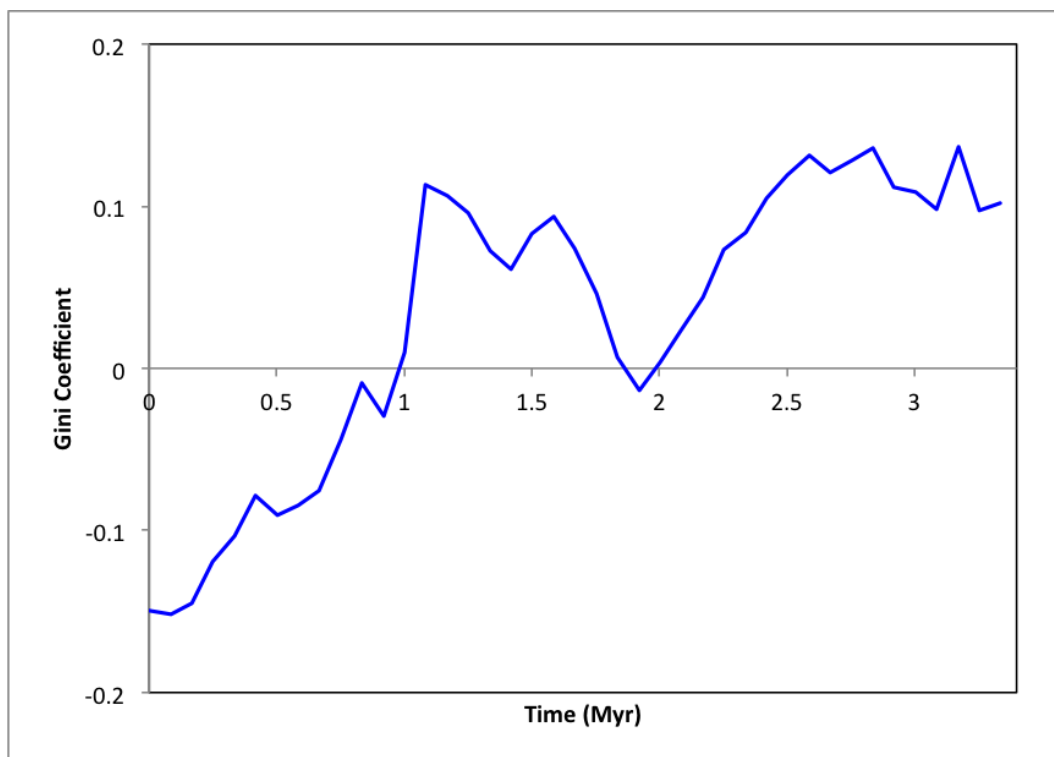
Figure 3.3: Graph of the Gini coefficient (a measure of the mass segregation of the cluster where $G \leq 0$ indicates a lack of mass segregation, while $G > 0$ indicates the presence of mass segregation) as a function of time for the run shown in Figures 3.1 and 3.2.

particles within a radius) and the cumulative fractional mass f_M (fraction of mass within a radius) though the equation:

$$G = 2 \int_0^1 (f_M - f_N) df_N \qquad (3.3)$$

If the mass is centrally concentrated, then $f_M \geq f_N$ at all radial distances and so $G \geq 0$. If the larger masses are located further from the centre, then $G < 0$.

This panel also shows the ring structures created in the gas, on either side of the x = 0 axis. These rings expand outwards from the core, though not perfectly symmetrically, and seem to be pushing some of the gas mass toward the edges of the cluster and away from the central core. As there is no stellar feedback activated in this model, these rings are a result of dynamics, hydrodynamics and shocks. Since these rings originate along the edge of the central spherical gas density, it is possible that something occurred at these locations and the rings are 'shockwaves' emanating from the event. The shape of the rebound effect is still visible in the overall shape of the cloud.

In panel 3.1d), we have the snapshot of the model at 2.75 Myr. We can see that the stars have relaxed into a more spherical central shape. In Figure 3.4, the ellipticity of the cluster is shown to decrease as a function of time. Although the entirety of the cluster still appears elliptical (the stars furthest from the centre are close to the z = 0 line), when the density contours are calculated using the R package, the cluster core is much more spherical. If we compare this panel to Figure 3.2d), which is the same timestamp but rotated 90 degrees to see the XY plane, we can easily see how much

more these two panels resemble each other than the a) panels of Figures 3.1 and 3.2.

There is also more evidence of the ring structures in the gas, with the remnants of more rings having been created in the core and dissipated by the time they reach the edge of the cloud (when they no longer have sufficient density to be easily discernable at this scale). These rings are also visible in Figure 3.2, which implies (since these snapshots are all slices along the central axes) that the rings are relatively spherical in three dimensions. The central gas core is also still visible, though significantly smaller than in the previous snapshot, and the shape of the rebound effect is mostly lost to a smooth spherical distribution at the edges of the cloud.

3.4.2   75% gas mass

In Figure 3.5, we have the snapshots taken of the XZ plane for the model with a gas mass fraction of 75% at the timesteps 0.0, 0.75, 1.75 and 2.75 Myr. When the gas mass fraction of the total mass is increased from 50% to 75%, some changes were apparent.

The initial conditions of position and velocities remained the same, so panel 3.5a) still greatly resembles panel 3.1a), though the gas is much more diffuse at the edges with the higher gas mass.

In panel 3.5b), we have the snapshot of the model at 0.75 Myr. It can be seen that the stars are still drawn gravitationally toward the core as we saw in the previous model, while a slightly larger percentage of stars ($\sim 5\%$) moved away from the cluster
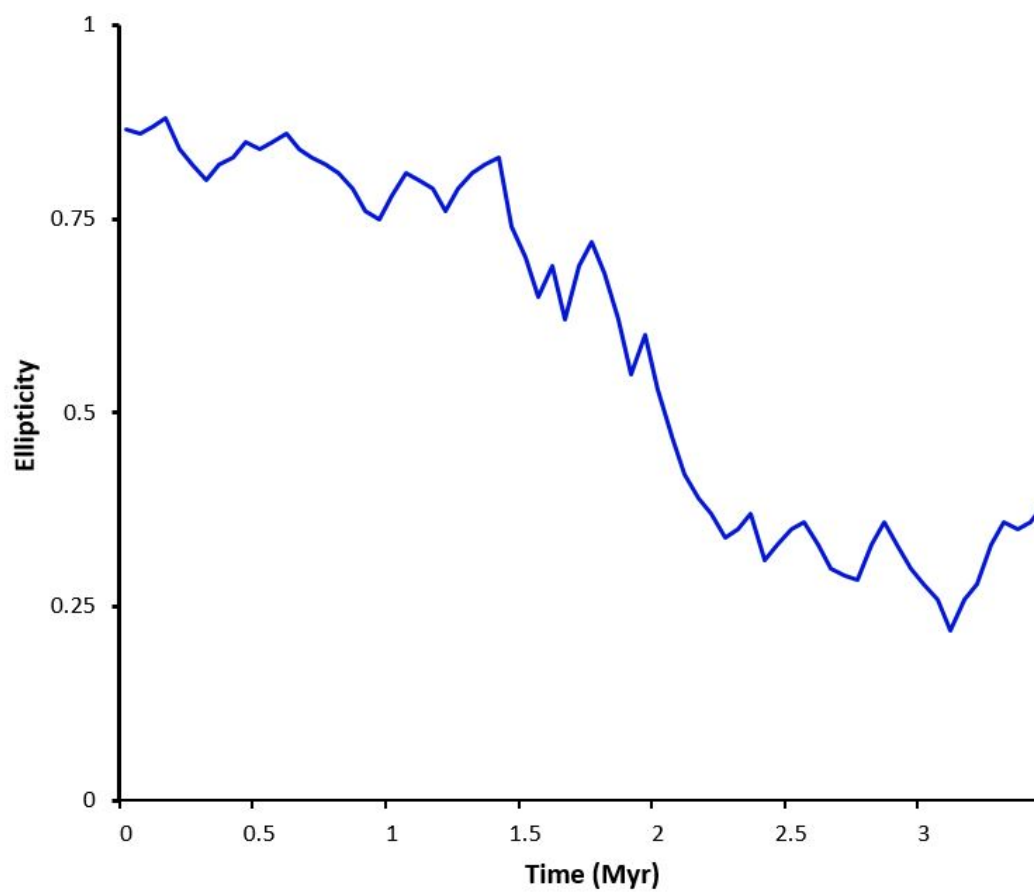
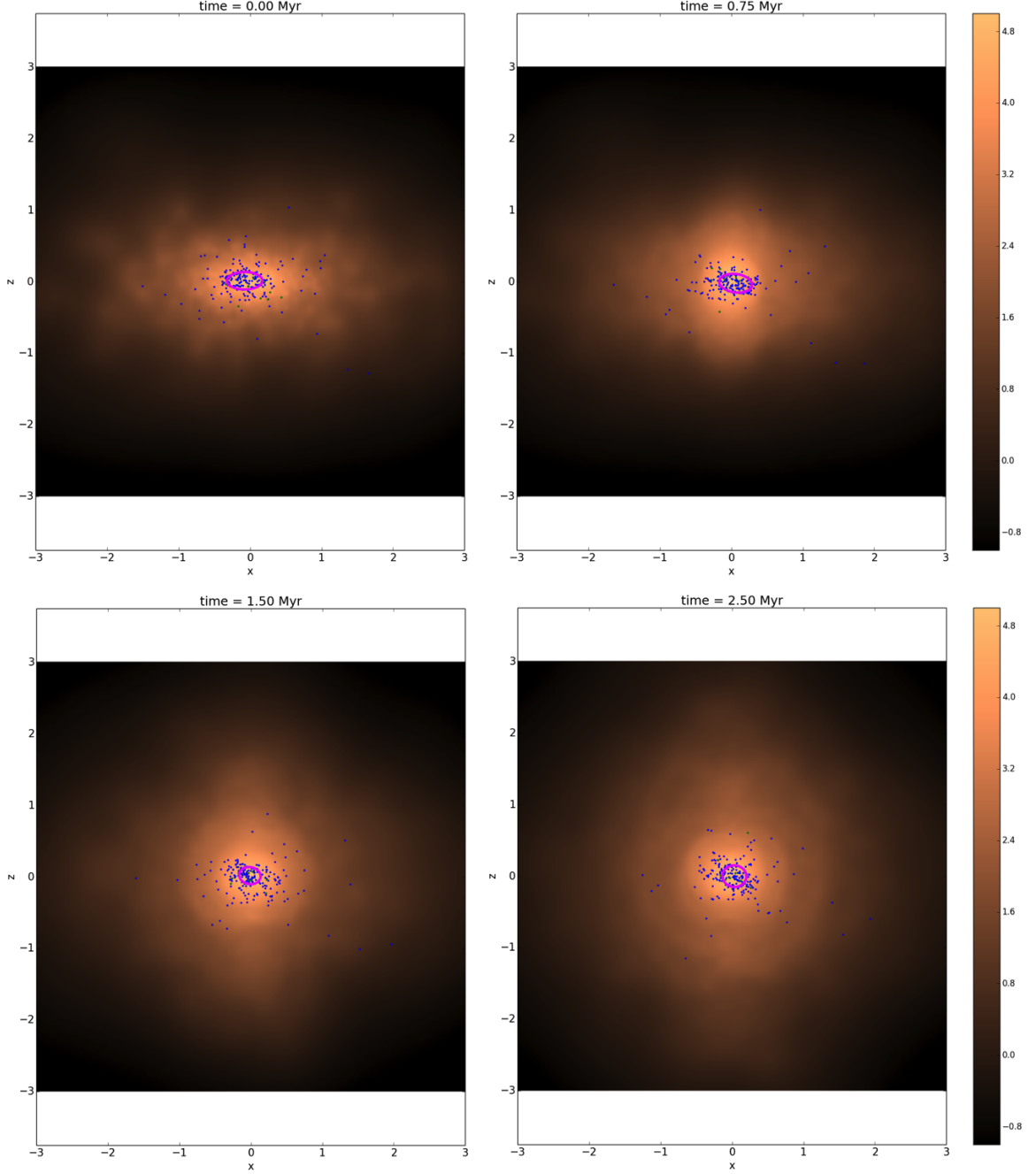Figure 3.4: Graph of the ellipticity of the cluster as a function of time for the run shown in Figures 3.1 and 3.2.

Figure 3.5: Snapshots of the XZ plane of the $f_{gas} = 0.75$ model at 0.0, 0.75, 1.75 and 2.75 Myr. Blue points are stars with $M < 0.9 M_\odot$, green points have $0.9\ M_\odot < M < 2.5 M_\odot$ and red points have $2.5 M_\odot < M < 10 M_\odot$. The pink oval shows the ellipticity of the core. Also shown is the gas density plot.

edges. The gas still forms a central density, and with the higher gas mass, the size and mass of this central density is also larger with a radius of 0.4 pc. The rebound effect is still visible, though slightly obscured by the higher density of the gas still in the elliptical formation.

In panel 3.5c), we have the snapshot of the model at 1.75 Myr. At this point, the ellipticity of the star cluster is less than that of the previous model, so it is obtaining its spherical shape at a faster rate with the higher gas mass. This could be due to the larger dense core of gas at the centre of the cluster that forms more quickly than the star distribution. In addition, the stars seem to cluster more densely at the core where the gas is also densest and the stars are less likely to leave the cluster. Future work may tell us if the additional mass at the centre of the cluster affects the gravitational pull on the outer stars enough to effect these changes.

There does not exist as distinct the ring structures in the gas cloud with higher gas mass, though they are still present. Once again, this lack of visibility is partially due to the overall increase in density of the gas, making the shapes less distinct. Also, these structures appear much more spherical than in Figure 3.5c), and like with the stars, it is possible that this is due to the gravitational effects of the larger gas core. Alternately, it could be due to the more random effect of the ring generating events occurring closer to the centre of the gas core, allowing for a more even shock through the cloud.

In panel 3.5d), we have the snapshot of the model at 2.75 Myr. The stars maintain their more spherical shape, with only minor fluctuations in the core radius. The ring

structures are still visible and more numerous as time goes on, just as in Figure 3.1d).

3.4.3 Stars

From the previous two sections, we can see that as the model evolves, the ellipticity of the stellar core decreases and the cluster becomes more spherical.

By ~ 2.0 Myr, the initial ellipticity of the stars is no longer as obvious to the naked eye. When comparing the XY view to the XZ view, it is not easy to differentiate the initially spherical setup of the XY plane from the initially elliptical setup of the XZ plane.

By ~ 3.5 Myr, some of the outer stars appear to be leaving the cluster or at least dissipating outward. Some have slowed enough to create a cluster in the XZ view that more closely resembles a normal Plummer sphere. Some have enough speed that they will eventually leave the cluster entirely (generally only between 3-5 stars per run).

It is interesting to note that the stars move at a much slower pace than the gas as a *set*, but have in general a *larger* velocity when comparing *particles*. Stars have a mean velocity of ~ 1 km/s at ~ 3.5 Myr while gas only has mean velocity of ~ 0.2 km/s at the same timestamp.

The stars furthest from the core of the cluster move toward the centre of mass ($x \approx y \approx z \approx 0$), with the furthest large star (mass $> 2.5 M_\odot$) reaching the centre at ~ 2.0 Myr (we mention the largest stars because they are easy to identify on

snapshots, being both few and a distinct colour). This is expected, due to mass segregation. The motions of the stars initially closer to the core are much more randomized, not merely collapsing toward the core.

3.4.4   Gas

From the sections 3.4.1 and 3.4.2, we can see that the ellipticity of the gas changes with time as there is a rebound effect causing a secondary ellipticity at a 90 degree angle from the initial set up. After this rebound, the gas starts to form a dense core at the centre of the cluster, spherical in shape.

An unexpected occurrence was the formation of visible ring patterns in the gas at ~ 1.50 Myr (see Figure 3.1c)) that expand outward from the core. This was not a singular occurrence as secondary rings form from the core at ~ 2.5 and ~ 3.5 Myr in each of the runs. The mechanisms of gas expulsion from young clusters are still unclear, though supernovae and stellar feedback as well as star formation are amongst the possibilities (Dale et al., 2015; Pfalzner and Kaczmarek, 2013). If these rings of outwardly moving gas are in fact removing gas mass from the cluster, it is possible that dynamics, hydrodynamics and shocks may also play a role in gas expulsion.

Chapter 4

Discussion & Conclusion

4.1 Comparison with MYStIX

What do these simulations and results mean in comparison to the MYStIX results and other known information about clusters?

Older open clusters are known to be spherical in shape and have very little gas remaining. Our results suggest that when starting with a young highly elliptical cluster, it is possible that the cluster would evolve into a much more spherical cluster within 5 Myr through pure dynamics. This could mean that the very young elliptical cluster of the MYStIX project could later evolve into the spherical older clusters we see elsewhere in the galaxy.

A large portion of the MYStIX clusters were found to have some ellipticity (see Figure 1.3), which could imply that a significant portion of all young clusters began

in a similar formation. Our model shows that if that is the case, within a few million years it would be difficult to distinguish these formerly elliptical clusters from clusters that were spherical from their formation. Also, we show that elliptical clusters do not merely dissipate due to their irregular shape, and that the uniformity of their older counterparts maybe be due to dynamical interactions.

However, the timing of it does not all quite match. There are MYStIX clusters older than 2 Myr that still have ellipticity present in the stars, such as the Carina Nebula at the age of 1.5-4 Myr (Getman et al., 2014) with subcluster ellipticities in the range of 0.2-0.8, but the majority of the clusters are under 2 Myr, so it is possible that by the time star formation ended (or slowed down), it has not been long enough for the stars to relax into a spherical shape. It would be useful in the future to have star formation and evolution integrated into the code in order to get a better understanding of how these factors can affect the model, especially at the beginning of the run time.

Another possibility is that other factors are keeping the subclusters in elliptical shape, such as rotation, and inflows and outflows of gas. The latter is especially likely, as many of the subclusters formed along a filament of gas, allowing the movement of gas through the clusters along a known route. Knowing accurate velocities for stars would tell us a lot about the movements of the subclusters as a whole and about the movements of the stars within the subcluster. A particular topic of interest is investigating whether or not the multiple subclusters, in various patterns as described in Section 1.2.2, eventually coalesce into a single bound cluster, as generally open clusters are singular objects and not the loose association of multiple subclusters.

This could be done with this AMUSE framework by initializing multiple clusters of stars and gas, then giving each subcluster a general velocity, as well as the more random peculiar velocities of the individual stars.

4.2   Mass Segregation & Gas Expulsion

It was encouraging to see that mass segregation occurs gradually in this model, as this is what is expected when stars with a known IMF are randomly placed in a cluster. Also, that the vast majority of the stars remained bound to the cluster, with very few stars randomly obtaining enough velocity to be ejected, as we started with a bound system and there were no known high energy events beyond two-body interactions.

Open clusters have little to no gas, but these very young MYStIX clusters have an abundance of it. While it is not known exactly how these clusters lose their gas, it is thought to occur fairly early on in the cluster's evolution and could have an effect on the evolution of the structure of the stars within the cluster (Pfalzner and Kaczmarek, 2013). So it is important to look at how the gas behaves within our model in order to determine if there is a method of gas expulsion present.

It appears that even without star formation, stellar feedback or supernovae, it is possible that the gas is being slowly dispersed from the cluster through dynamics. The ring structures seen in Figures 3.3 and 3.5 could be waves of gas being pushed out of the core and into the edges of the cluster where they could be more easily taken away.

It is unknown what were the triggering events of these rings, as they occurred multiple times in every run, but at different times and creating slightly different patterns. Since not all the rings were centred at the centre of the gas density, but almost always near the core of the cluster, it is possible that a stellar interaction could be what injected enough energy into the system to create the rings. Alternately, these shocks could be a purely gaseous phenomenon, brought on by the high concentration of gas at the centre of the cluster. This was an unexpected effect, but one of great interest. This gas expulsion could not happen on a fast enough timescale to completely strip a cluster of its gas as the only mechanism, but it is a possibility as just one component of the process.

It is important to try to solve this problem of gas expulsion, since we have seen the mass of the gas present in the cluster does have a visible effect on the evolution of the cluster, allowing the cluster to lose its ellipticity at a faster rate, and this effect could be even greater with the presence of star formation and evolution.

The 'rebound effect' seen in Figures 3.1b) and 3.5b) is also of interest. Gas from both far ends of the cluster (furthest from the core) is drawn toward the core through gravity, but when these two 'waves' of gas collide, they cannot merely pass by and through one another due to the high number of particles and density. Since the strongest forces are coming from the ends, it is easiest for the gas particles to instead move perpendicularly along the YZ plane (as when a gas is blown against a flat unmoving surface, it spreads out in a circular shape around the point of contact), giving the bulge seen in the gas density plot.

4.3   Future Work

Our work has demonstrated the plausibility of a young elliptical cluster evolving into a spherical cluster within a few million years. Since almost all of the large star-forming regions in the MYStIX project were formed of many small elliptical subclusters, it is of great interest to investigate how those subclusters interact with each other, if they amalgamate into one large open cluster or remain distinct. This could be accomplished by initializing multiple instances of our model with predetermined distances between the cores, then evolving for millions of years.

Another area of future interest is investigating how the gas is expelled from the young cluster, as discussed in the previous section. Possibilities include adding stellar feedback, supernovae and star formation to the code, allowing the gas to have more interactions with both itself and the stars.

Bibliography

L. Allen, S. T. Megeath, R. Gutermuth, P. C. Myers, S. Wolk, F. C. Adams, J. Muzerolle, E. Young, and J. L. Pipher. The Structure and Evolution of Young Stellar Clusters. *Protostars and Planets V*, pages 361–376, 2007.

R. J. Allison, S. P. Goodwin, R. J. Parker, R. de Grijs, S. F. Portegies Zwart, and M. B. N. Kouwenhoven. Dynamical Mass Segregation on a Very Short Timescale. *ApJL*, 700:L99–L103, 2009.

A. W. Appel. An Efficient Program for Many-Body Simulation. *SIAM Journal on Scientific and Statistical Computing, vol. 6, no. 1, January 1985, p. 85-103.*, 6: 85–103, 1985.

J. Barnes and P. Hut. A hierarchical O(N log N) force-calculation algorithm. *Nature*, 324:446–449, 1986.

N. Bastian and S. P. Goodwin. Evidence for the strong effect of gas removal on the internal dynamics of young stellar clusters. *MNRAS*, 369:L9–L13, June 2006.

J. Binney and S. Tremaine. *Galactic Dynamics: Second Edition.* Princeton University Press, 2008.

P. S. Broos, K. V. Getman, M. S. Povich, E. D. Feigelson, L. K. Townsley, T. Naylor, M. A. Kuhn, R. R. King, and H. A. Busk. Identifying Young Stars in Massive Star-forming Regions for the MYStIX Project. *ApJS*, 209:32, Dec. 2013.

A. Burkert. Star Formation in Turbulent Molecular Clouds (Review). In E. K. Grebel and W. Brandner, editors, *Modes of Star Formation and the Origin of Field Populations*, volume 285 of *Astronomical Society of the Pacific Conference Series*, page 3, 2002.

A. Burkert and L. Hartmann. Collapse and Fragmentation in Finite Sheets. *ApJ*, 616:288–300, 2004.

S. Chandrasekhar. *Principles of stellar dynamics.* The University of Chicago Press, 1942.

J. M. Converse and S. W. Stahler. The Distribution of Stellar Mass in the Pleiades. *ApJ*, 678(1):431, 2008.

J. E. Dale, B. Ercolano, and I. A. Bonnell. Early evolution of embedded clusters. *MNRAS*, Apr. 2015.

B. G. Elmegreen. Star Formation in a Crossing Time. *ApJ*, 530:277–281, 2000.

E. D. Feigelson. X-ray insights into star and planet formation. *Proceedings of the National Academy of Science*, 107:7153–7157, 2010.

E. D. Feigelson, L. K. Townsley, P. S. Broos, H. A. Busk, K. V. Getman, R. R. King, Kuhn], M. A. and Naylor, T. and Povich, M. S., A. Baddeley, M. R. Bate, R. Indebetouw, K. L. Luhman, M. J. McCaughrean, J. M. Pittard, R. E. Pudritz, A. Sills, Y. Song, and J. Wadsley. Overview of the Massive Young Star-Forming Complex Study in Infrared and X-Ray (MYStIX) Project. *ApJS*, 209:26, 2013.

M. Fujii, M. Iwasawa, Y. Funato, and J. Makino. BRIDGE: A Direct-Tree Hybrid N-Body Algorithm for Fully Self-Consistent Simulations of Star Clusters and Their Parent Galaxies. *PASJ*, 59:1095–, 2007.

M. S. Fujii, T. R. Saitoh, and S. F. Portegies Zwart. The Formation of Young Dense Star Clusters through Mergers. *ApJ*, 753:85, July 2012.

Y. Fukui. Molecular Clouds and Star Formation in the Local Group (Review). In E. K. Grebel and W. Brandner, editors, *Modes of Star Formation and the Origin of Field Populations*, volume 285 of *Astronomical Society of the Pacific Conference Series*, page 24, 2002.

K. V. Getman, E. D. Feigelson, P. S. Broos, L. K. Townsley, and G. P. Garmire. Methods for Estimating Fluxes and Absorptions of Faint X-ray Sources. *ApJ*, 708: 1760–1771, Jan. 2010.

K. V. Getman, E. D. Feigelson, M. A. Kuhn, P. S. Broos, L. K. Townsley, T. Naylor, M. S. Povich, K. L. Luhman, and G. P. Garmire. Age Gradients in the Stellar Populations of Massive Star Forming Regions Based on a New Stellar Chronometer. *ApJ*, 787:108, 2014.

R. Gingold and J. J. Monaghan. Kernel estimates as a basis for general particle methods in hydrodynamics. *J. Comput. Phys.*, 46(3):429 – 453, 1982.

R. A. Gutermuth, S. T. Megeath, P. C. Myers, L. E. Allen, J. L. Pipher, and G. G. Fazio. A Spitzer Survey of Young Stellar Clusters Within One Kiloparsec of the Sun: Cluster Core Extraction and Basic Structural Analysis. *ApJS*, 184:18–83, Sept. 2009.

L. Hernquist. Hierarchical N-body methods. *Comp. Phys. Comm.*, 48:107–115, 1988.

R. W. Hockney and J. W. Eastwood. *Computer simulation using particles*. Bristol: Hilger, 1988, 1988.

C. S. Howard, R. E. Pudritz, and W. E. Harris. Cluster formation in molecular clouds - I. Stellar populations, star formation rates and ionizing radiation. *MNRAS*, 438: 1305–1317, Feb. 2014.

P. Hut, J. Makino, and S. McMillan. Building a better leapfrog. *ApJL*, 443:L93–L96, 1995.

G. R. Johnson. Artificial viscosity effects for SPH impact computations. *Int. J. of Impact Eng.*, 18(5):477 – 488, 1996.

M. A. Kuhn, K. V. Getman, E. D. Feigelson, A. Baddeley, L. K. Townsley, P. S. Broos, A. Sills, M. R. Bate, M. S. Povich, K. L. Luhman, H. A. Busk, T. Naylor, R. R. King, and Y. Song. The Spatial Structure of Young Stellar Clusters. I. Subclusters. *ApJ*, 787:107, 2014.

C. J. Lada and E. A. Lada. Embedded Clusters in Molecular Clouds. *ARAA*, 41: 57–115, 2003.

D. Leisawitz, F. N. Bash, and P. Thaddeus. A CO survey of regions around 34 open clusters. *ApJS*, 70:731–812, Aug. 1989.

L. B. Lucy. A numerical approach to the testing of the fission hypothesis. *AJ*, 82: 1013–1024, 1977.

J. Makino. Optimal order and time-step criterion for Aarseth-type N-body integrators. *ApJ*, 369:200–212, 1991.

S. L. W. McMillan, E. Vesperini, and S. F. Portegies Zwart. A Dynamical Origin for Early Mass Segregation in Young Star Clusters. *ApJL*, 655:L45–L49, Jan. 2007.

N. Moeckel and M. R. Bate. On the evolution of a star cluster and its multiple stellar systems following gas dispersal. *MNRAS*, 404:721–737, 2010.

J. J. Monaghan. Smoothed particle hydrodynamics. *ARAA*, 30:543–574, 1992.

J. J. Monaghan. SPH and Riemann Solvers. *J. of Comp. Phys.*, 136(2):298 – 307, 1997.

J. J. Monaghan and J. C. Lattanzio. A refined particle method for astrophysical problems. *AAP*, 149:135–143, 1985.

F. I. Pelupessy, J. Jänes, and S. Portegies Zwart. N-body integrators with individual time steps from Hierarchical splitting. *NA*, 17:711–719, 2012.

F. I. Pelupessy, A. van Elteren, N. de Vries, S. L. W. McMillan, N. Drost, and S. F. Portegies Zwart. The astrophysical multipurpose software environment. *A&A*, 557: A84, 2013.

S. Pfalzner and P. Gibbon. *Many-body Tree Methods in Physics.* Cambridge University Press, 1996.

S. Pfalzner and T. Kaczmarek. Reaction of massive clusters to gas expulsion - The cluster density dependence. *AAP*, 555:A135, 2013.

S. Pfalzner, T. Kaczmarek, and C. Olczak. Modes of clustered star formation. *AAP*, 545:A122, 2012.

J. Pflamm-Altenburg and P. Kroupa. A highly abnormal massive star mass function in the Orion Nebula cluster and the dynamical decay of trapezium systems. *MNRAS*, 373:295–304, 2006.

H. C. Plummer. On the problem of distribution in globular star clusters. *MNRAS*, 71, 1911.

D. H. Porter. *A study of hierarchical clustering of galaxies in an expanding universe.* PhD thesis, California Univ., Berkeley., 1985.

J. K. Salmon, M. Warren, and G. Winckelmans. Fast Parallel Tree Codes for Gravitational and Fluid Dynamical N-Body Problems. *Int. J. Supercomp. Appl. High Perf. Comp.*, 8:129–142, 1994.

E. E. Salpeter. The Luminosity Function and Stellar Evolution. *ApJ*, 121:161, 1955.

V. Springel. The cosmological simulation code GADGET-2. *MNRAS*, 364:1105–1134, 2005.

V. Springel. Smoothed Particle Hydrodynamics in Astrophysics. *ARAA*, 48:391–430, 2010.

V. Springel and L. Hernquist. Cosmological smoothed particle hydrodynamics simulations: the entropy equation. *MNRAS*, 333:649–664, 2002.

J. C. Tan, M. R. Krumholz, and C. F. McKee. Equilibrium Star Cluster Formation. *ApJL*, 641:L121–L124, 2006.

J. Wisdom and M. Holman. Symplectic maps for the n-body problem. *AJ*, 102: 1528–1538, 1991.